RESEARCH ARTICLE | JULY 12 2023

Two-phase flow simulations of surface waves in wind-forced conditions •

Malte Loft **№** (a); Niklas Kühl (b); Marc P. Buckley (b); Jeffrey R. Carpenter (c); Michael Hinze (c); Fabrice Veron (d); Thomas Rung (d)



Physics of Fluids 35, 072108 (2023) https://doi.org/10.1063/5.0156963





Articles You May Be Interested In

Numerical investigation of the interaction between an interface and a decaying Lamb-Oseen vortex

Physics of Fluids (July 2024)

Phase field lattice Boltzmann model for air-water two phase flows

Physics of Fluids (July 2019)

Hydrodynamic performance of a highly-skewed propeller in ventilated flow conditions near the free surface

Physics of Fluids (January 2025)



Physics of Fluids

Special Topics Open for Submissions

Learn More



Two-phase flow simulations of surface waves in wind-forced conditions of surface waves

Cite as: Phys. Fluids 35, 072108 (2023); doi: 10.1063/5.0156963

Submitted: 4 May 2023 · Accepted: 23 June 2023 ·

Published Online: 12 July 2023







Malte Loft,^{1,a)} (D Niklas Kühl,¹ (D Marc P. Buckley,² (D Jeffrey R. Carpenter,² (D Michael Hinze,³ (D Fabrice Veron,⁴ (D and Thomas Rung¹ (D

AFFILIATIONS

Institute for Fluid Dynamics and Ship Theory, Hamburg University of Technology, Am Schwarzenberg-Campus 4, D-21075 Hamburg, Germany

ABSTRACT

The paper is devoted to two-phase flow simulations and investigates the ability of a diffusive interface Cahn-Hilliard volume-of-fluid model to capture the dynamics of the air-sea interface at geophysically relevant Reynolds numbers. It employs a hybrid filtered/averaging improved detached eddy simulation method to model turbulence and utilizes a continuum model to account for surface tension if the diffuse interface is under-resolved by the grid. A numerical wind-wave tank is introduced, and results obtained for two known wind-wave conditions are analyzed in comparison to experimental data at matched Reynolds numbers. The focus of the comparison is on both time-averaged and wave-coherent quantities, and includes pressure, velocity as well as modeled and resolved Reynolds stresses. In general, numerical predictions agree well with the experimental measurements and reproduce many wave-dependent flow features. Reynolds stresses near the water surface are found to be especially important in modulating the critical layer height. It is concluded that the diffusive interface approach proves to be a promising method for future studies of air-sea interface dynamics in geophysically relevant flows.

© 2023 Author(s). All article content, except where otherwise noted, is licensed under a Creative Commons Attribution (CC BY) license (http://creativecommons.org/licenses/by/4.0/). https://doi.org/10.1063/5.0156963

I. INTRODUCTION

The momentum and mechanical energy fluxes across the air–sea interface are an essential component of the global energy budget. It has been estimated that over 80% of the kinetic energy within the ocean originates from the mechanical action of the wind upon the wavy ocean surface.¹ These fluxes are controlled by the small-scale processes within the coupled atmospheric and oceanic wave boundary layers.² Global circulation models are not able to resolve these small-scale processes and rely on parameterizations of the wind stress. The parameterizations quantify both pressure drag and viscous stress contributions, whose influence depends on the specific wind-wave conditions. Moreover, the pathways leading to the partitioning of wind energy into wave growth, wave breaking, and current generation remain poorly understood.² At the same time, the influence of individual wave field parameters on the airflow dynamics is also unexplained. This is due, in part, to the technical challenges involved in observing

and simulating the physics in the fairly thin, dynamic two-phase flow regime of the wavy boundary layer, rendering detailed experiments or numerical simulations challenging.

From a numerical viewpoint, previous investigations were mostly restricted to single-phase approaches, where the air phase was predominantly studied. Such aerodynamic simulations specify a given mean free surface evolution, e.g., a plane progressive surface wave train. The (mean) free surface behavior is either obtained from precursor hydrodynamic simulations,³ (semi-)analytical descriptions based on empirically confirmed statistics,⁴ or simpler analytical expressions, e.g., Stokes waves as discussed in Yang and Shen.⁵ Results of these "one-way" couplings between a prescribed water phase and a simulated air phase show that the relation between the sea state and the wind stresses remains uncertain in high wind conditions, where nonlinear turbulent processes are dominant.⁶ Moreover, frequently employed interface descriptions, such as roughness-supported law-of-the-wall expressions, must be adjusted

²Institute of Coastal Ocean Dynamics, Helmholtz-Zentrum Hereon, Max-Planck-Straße 1, D-21502 Geesthacht, Germany

³Modeling, Simulation and Optimization of Complex Systems, Universität Koblenz-Landau, Universitätsstraße 1, D-56070 Koblenz, Germany

⁴School of Marine Science and Policy, University of Delaware, Newark, Delaware 19716, USA

^{a)}Author to whom correspondence should be addressed: malte.loft@tuhh.de

to wave parameters—for example, to the wave steepness or the wave age—to alter the roughness of the free surface and thereby the surface stress. However, despite comprehensive parameterizations of the atmospheric boundary layer and the related drag coefficient, the physical processes acting in the atmospheric and oceanic wavy boundary layers are not well known.²

Single-phase aerodynamic simulations benefit from superior efficiency and an inherently sharp interface. However, the benefits come at the expense of an assumed sea state and hypothesized turbulent interface physics. This limits the air-sea flux simulation capabilities and motivates a two-phase flow framework. Mesh-based computational approaches for immiscible two-phase flows mainly refer to interface-capturing methods that reconstruct the free surface position from an indicator function. Within the class of interface-capturing methods, the volume-of-fluid (VoF) approach of Hirt and Nichols⁸ is predominantly used. The method is conservative and capable of predicting (incipient) wave breaking and related influences on the generation of turbulence, vorticity, and ocean current, for example, as discussed by Perlin, Choi, and Tian. Breaking waves were previously simulated but with less attention to wind-wave interaction. Examples are found in Iafrati^{10,11} or Lubin and Glockner,¹² who presented the first large eddy simulation (LES) results obtained by a VoF approach for a plunging breaking wave problem. The latter study was confined to the generation of dissipative vortical structures under breaking waves. With attention given to technical ocean engineering flows, Hu et al. 13 reported good agreement between simulations and measurements for investigations of different breaking wave impacts on structures using a VoF method in combination with a Reynolds averaged turbulence model. Employing a similar VoF method, Hao et al. 14 reported direct numerical simulation (DNS) results for wind over breaking waves scenarios. Most previous two-phase flow simulations did neglect capillary effects, which might be of interest for wind-wave interaction simulations, as indicated by the pronounced sensitivity to the roughness model outlined in Husain et al. An exception is the work of Deike, Popinet, and Melville¹⁵ and Wu, Popinet, and Deike.¹⁶ In the latter, similar wave parameters as in this study were investigated with a VoF method. Due to the Reynolds number limitations imposed by DNS, the investigated Reynolds numbers Re_i \approx 200 are, however, significantly smaller than in this paper, which reaches up to Re $_{\lambda} \approx 20~000$, cf. Table I. Here, the Reynolds number Re₂ is defined by

$$Re_{\lambda} = \frac{\rho_{air} u_* \lambda_p}{\mu_{air}} \tag{1}$$

with $\rho_{\rm air}$, $\mu_{\rm air}$, u_* , and $\lambda_{\rm p}$ representing the density and dynamic viscosity of the air as well as the friction velocity and peak wavelength.

An alternative to the VoF approach is the diffuse phase field model suggested by Cahn and Hilliard (CH). In contrast to VoF methods, the Cahn–Hilliard (CH) approach models the phase separation of immiscible fluids and naturally incorporates surface tension/capillary effects, which is why a related empirical model, such as the popular continuum method suggested by Brackbill, Kothe, and Zemach, is not necessarily required for interface resolving simulations. There exists a variety of CH models for two-phase flows. Examples refer to fluids with matched densities described in Hohenberg and Halperin, identical viscosities outlined by Jacqmin, or thermodynamically consistent approaches (cf. Refs. 21–23).

The present research aims at simulations of the air–sea interface along a route outlined in Eden and Iske, ²⁴ i.e., using a CH–VoF approach published in Kühl, Hinze, and Rung. ²⁵ The model bridges VoF and CH concepts and can be used for different levels of interface resolution, i.e., in combination with implicit (CH-based) surface tension models in the resolved case, or explicit surface tension models in an under-resolved case. The two-phase approach is implemented into an implicit, multi-phase finite-volume (FV) method using unstructured grids and a free surface adapted detached eddy simulation framework (DES; Ref. 26) to model turbulence.

The paper is structured as follows: Sec. II introduces the computational model, including the building blocks specific to the two-phase flow treatment. Subsequently, the triple decomposition, originally suggested in Phillips, ²⁷ utilized to process the computed spatiotemporal results is described in Sec. III. Section IV is devoted to a simple verification study of the post-processing routine. Applications for two different experimentally reported wind–wave scenarios are presented in Sec. V. The results include instantaneous fields, wave coherent, and averaged quantities as well as turbulent stresses in comparison with the experimental data. Final conclusions and future directions are outlined in Sec. VI. Within the publication, Einstein summation convention is used for lower-case Latin subscripts. Vectors and tensors are defined with reference to Cartesian coordinates. A list of symbols is briefly provided at the end of this paper.

II. COMPUTATIONAL MODEL

The computational model consists of four essential building blocks. The baseline FV procedure is briefly discussed in Sec. II A. The employed two-phase flow model and the hybrid filtered/averaged turbulence closure are outlined in Secs. II B and II C. Finally, a numerical wind—wave tank is introduced in Sec. II D.

A. Numerical procedure

The numerical procedure utilizes an FV approximation dedicated to single instruction multiple data (SIMD) implementations on a

TABLE I. Summary of assessed wind—wave conditions for scenarios I and II (III), where a_p refers to the characteristic peak amplitude, λ_p denotes the related peak wavelength, k_p is the peak wave number, and f_p refers to the peak frequency of the measured (simulated) waves. These parameters were extracted from a somewhat broader spectrum reported by Buckley and Veron, ⁴¹ cf. Fig. 2. The air phase is characterized by the "10 m" wind speed u_{10} , the friction velocity u_* along the air–sea interface, and the related roughness length z_0 . The wave age is characterized by C_p/u_* and the wave slope by a_pk_p . The Reynolds number is defined by $Re_\lambda = \rho_{air}u_*\lambda_p/\mu_{air}$.

Scenario	Descriptor	u ₁₀ (m/s)	a _p (cm)	λ _p (m)	f _p (Hz)	<i>u</i> _* (m/s)	z_0 (m)	$C_{\rm p}/u_*$	$a_{\mathrm{p}}k_{\mathrm{p}}$	Reλ
I	Low wind speed	2.19	0.15 (0.19)	0.14	3.3	0.07	3×10^{-5}	6.40	0.07 (0.09)	6×10^2
II	High wind speed	16.63	2.29 (2.40)	0.54	1.7	0.67	5×10^{-4}	1.37	0.27 (0.28)	2×10^4
(III)		9.41	1.20	0.39	2.0	0.31		2.50	0.19	7×10^3

distributed-memory parallel CPU machine. Algorithms employed by the in-house procedure FreSCo⁺ are described and validated for various applications in Rung *et al.*, ²⁸ Yakubov *et al.*, ²⁹ and Kühl *et al.* ³⁰ They ground on the integral form of a generic Eulerian transport equation, with residuum R^{φ} for a scalar field $\varphi(x_i, t)$ exposed to the influence of a possibly non-linear source \mathscr{S}^{φ} in addition to a modeled (non-linear) gradient diffusion term and its diffusivity Γ^{eff} in a control volume V bounded by the surface S(V), viz.,

$$\int_{V} \mathbf{R}^{\varphi} = 0, \quad \rightarrow \quad \int_{V} \left[\frac{\partial \varphi}{\partial t} - \mathscr{S}^{\varphi} \right] dV + \oint_{S(V)} \left[u_{i} \varphi - \Gamma^{\text{eff}} \frac{\partial \varphi}{\partial x_{i}} \right] n_{i} dS = 0.$$
(2)

Here, x_i refers to the Cartesian spatial coordinates, u_i denotes to the Cartesian components of the velocity vector, n_i features the face-normal vector, and t is the time. The sequential procedure uses the strong conservation form and employs a cell-centered, co-located storage arrangement for all transport properties. Spatial discretization assumes unstructured grids based on arbitrary polyhedral cells, which connect to a face-based data structure. Various turbulence-closure models are available with respect to (w.r.t.) statistical [Reynolds averaged Navier-Stokes (RANS)] or scale-resolving (LES, DES) approaches. The numerical integration refers to the mid-point rule. Diffusive fluxes are determined from second-order central differencing, and convective fluxes employ higher-order upwind biased interpolation formulas. An exception refers to the convection of the concentration field (cf. Sec. II B), which employs the compressive high resolution interface-capturing (HRIC) scheme published by Muzaferija and Peric³¹ as well as the inter gamma differencing scheme (IGDS) discussed by Jasak and Weller³² in conjunction with VoF simulations. In contrast, a computationally more robust first-order upwind scheme is used in conjunction with the CH-VoF method advocated in this paper. The time integration follows from an implicit, second-order accurate three-time level (ITTL) approach. The latter employs a parabolic Ansatz function in time, is frequently used in engineering approaches, and provides a fair compromise in terms of robustness and accuracy, cf. Ferziger, Peric, and Street,³³ pp. 165–166. Preconditioned Krylov-subspace solvers are used to solve the algebraic equation systems, and the global flow field is iterated to convergence using a pressure-correction scheme (SIMPLE). The procedure is parallelized using a domain decomposition method and the message passing interface (MPI) communication protocol.

B. Two-phase flow model

The computational model assumes two immiscible, inert fluids (a,b) featuring constant bulk densities (ρ_a,ρ_b) (kg/m³) and bulk viscosities (μ_a,μ_b) (N s/m²). Fluid a is referred to as foreground fluid, i.e., the air phase, and fluid b as background fluid, i.e., the water/sea phase. Both fluids are assumed to share the kinematic field along the route of the VoF-approach suggested by Hirt and Nichols.⁸ An Eulerian concentration field describes the spatial distribution of the fluids, where $c=c_a=V_{\rm air}/V$ denotes the volume concentration of the foreground fluid, and the volume fraction occupied by the background fluid refers to $c_b=V_{\rm sea}/V=(V-V_{\rm air})/V=(1-c)$.

1. Concentration transport

Since the material properties of immiscible, inert fluids are invariable when using the VoF-method, the concentration is governed by a

simple Lagrangian transport equation, i.e., $dc_a/dt = -dc_b/dt$ = dc/dt = 0, which is translated into an Eulerian formulation before its discretization. On the contrary, diffuse interface methods replace the sharp interface with a thin layer where the fluids exchange mass fluxes. Cahn–Hilliard approaches can be separated into mass and volume conservative strategies and essentially augment the Lagrangian concentration transport by a velocity-divergence term and a non-linear, diffusive right-hand side (RHS) of order four, that vanishes outside the interface region, cf. Ding, Spelt, and Shu³⁴ and Kühl, Hinze, and Rung, ²⁵ viz.,

$$\frac{\mathrm{d}c}{\mathrm{d}t} = \frac{\partial}{\partial x_k} \left[M \frac{\partial \psi}{\partial x_k} \right] - c \frac{\partial u_k}{\partial x_k} \quad \to \quad \frac{\partial c}{\partial t} + \frac{\partial u_k c}{\partial x_k} = \frac{\partial}{\partial x_k} \left[M \frac{\partial \psi}{\partial x_k} \right]. \tag{3}$$

Here, $\psi(c, \partial^2 c/\partial x_k^2)$ (N/m²) is a chemical potential, and M(c) refers to a mobility parameter of dimension m⁴/(N s). Following Kühl, Hinze, and Rung,²⁵ the present study employs a mass conservative strategy together with an appropriate choice of M and a frequently used "double-well potential," which yields

$$\psi = 2C_1 \left[(2c^3 - 3c^2 + c) - 0.5 \left(\frac{C_2}{C_1} \right) \frac{\partial^2 c}{\partial x_k^2} \right],$$
 (4)

$$\frac{\partial \psi}{\partial x_k} = 2C_1 \left[(6c^2 - 6c + 1) \frac{\partial c}{\partial x_k} - 0.5 \left(\frac{C_2}{C_1} \right) \frac{\partial^3 c}{\partial x_k^3} \right]. \tag{5}$$

Two parameters are involved in the definition of the chemical potential ψ . These read $C_1=\sigma/\gamma$ and $C_2=\sigma\gamma$, and both employ the surface tension σ (N/m) and the interface thickness γ (m). The ratio $C_2/C_1\sim\gamma^2$ scales with the square of the interface thickness. Moreover, the product $C_1\,M\sim\nu_c$ (m²/s) in (3) describes a nonlinear apparent viscosity $\nu_c=2C_1\cdot M(6c^2-6c+1)$. Evaluating the last term of $\partial\psi/\partial x_k$ in (5) requires sufficient grid resolution, i.e., the term can be neglected when the interface is under-resolved, which is the case in the present air–sea simulations. Mind that ν_c vanishes at $c=(0.5\pm\sqrt{3}/6)$ and is negative over approximately 58% of the inner transition regime between these roots, where it supports the phase separation process.

Though the non-zero RHS of (3) appears to increase the complexity, it is beneficial for various reasons. On the one hand, it facilitates more sound interface physics, e.g., naturally includes surface tension effects when the grid resolution adequately resolves the phase transition. On the other hand, the use of robust/stability-preserving, upwind-biased convective approximations is supported. The present applications are devoted to under-resolved studies. This allows one to cover larger spatiotemporal domains at higher Reynolds numbers but requires surface tension effects to be modeled by an auxiliary model, e.g., as described in Eq. (17).

2. Equation of state

An equation of state (EoS) is used to extract the local flow properties from the concentration field, the bulk properties and a non-dimensional function m(c), viz.,

$$\rho = m^{\rho} \rho^{\Delta} + \rho_{\rm h} \quad \text{and} \quad \mu = m^{\mu} \mu^{\Delta} + \mu_{\rm h},$$
(6)

where $\rho^{\Delta} = \rho_a - \rho_b$, $\mu^{\Delta} = \mu_a - \mu_b$ mark the respective bulk property differences. Although this is not necessary, the paper assigns

 $m^{\mu}=m^{\rho}$. Provisions on the EoS considered in this study aim to exclude nonphysical, unbounded density states by restricting $m\in[0,1]$ and to recover the single-phase limit states, i.e., m(c=1[0])=1[0], as discussed in Kühl, Hinze, and Rung.²⁵ The simplest conceivable EoS $m^{(1)}$ corresponds to a bounded linear interpolation between the limit states and is usually employed by VoF methods. More advanced alternatives $m^{(2)}$ and $m^{(3)}$ follow a hyperbolic tangent rule or its linearized version and employ a user-specified non-dimensional transition parameter $\gamma^{\rm m}$, viz.,

$$m^{(1)} = \begin{cases} 0 & \text{if } c < 0, \\ 1 & \text{if } c > 1, \\ c & \text{otherwise} \end{cases}$$
 (7)

as well as

$$m^{(2)} = \frac{1}{2} \left[\tanh\left(\frac{2c-1}{\gamma^{\mathrm{m}}}\right) + 1 \right]$$

or

$$m^{(3)} = \begin{cases} 0 & \text{if } c < 0.5(1 - \gamma^{m}), \\ 1 & \text{if } c > 0.5(1 + \gamma^{m}), \\ \frac{2c + 1 - \gamma^{m}}{2\gamma^{m}} & \text{otherwise.} \end{cases}$$
(8)

The hyperbolic EoS complies only asymptotically with the limit states. Hence, an upper bound for the transition parameter reads $\gamma^{\rm m} \leq 0.5$ to limit the error w.r.t. the limit states below 0.1%. Mind that $m^{(3)}$ refers to a linearization of $m^{(2)}$ and is preferred in the present study due to the non-asymptotic characteristics.

In combination with a CH formulation, a hyperbolic EoS offers a decisive advantage for constructing a two-phase flow model that does not resolve the extremely thin interface and closely resembles the traditional VoF framework. Introducing the EoS (6) into the mass conservative continuity equation yields an expression for the divergence of the velocity field, viz.,

$$\frac{\partial \rho}{\partial t} + \frac{\partial u_k \rho}{\partial x_k} = 0 \quad \rightarrow \quad \frac{\partial u_k}{\partial x_k} = \frac{\dot{\rho}_a}{\rho_a} + \frac{\dot{\rho}_b}{\rho_b} = f^{\rho} \frac{\mathrm{d}c}{\mathrm{d}t}$$

with

$$f^{\rho} = \frac{-\rho^{\Delta}}{\rho} \frac{\partial m}{\partial c}.$$
 (9)

Here, $\dot{\rho}_a = -\dot{\rho}_b$ represents the mass transfer rates into phases a and b. Mass conservative CH formulations yield non-solenoidal velocity fields unless f^ρ vanishes. This, in turn, suggests employing the hyperbolic EoS $m^{(2)}$ or its linearized variant $m^{(3)}$, which can compress the non-solenoidal regime to a fairly small layer controlled by $\gamma^{\rm m}$.

To determine the thickness of the physical interface, the authors recommend to measure the density thickness within $\rho \in [1.05\rho_a, 0.95\rho_b]$ in a phase-averaged manner using wave following coordinates, cf. Sec. III B.

3. Governing equations

The governing equations primarily refer to the momentum and continuity equation for the mixture as well as a transport equation for the volume concentration of the foreground phase. They provide the pressure p, velocity u_p and volume concentration c, viz.,

$$R^{p} = \frac{\partial u_{k}}{\partial x_{k}} - \frac{f^{\rho}}{1 + f^{\rho}c} \frac{\partial}{\partial x_{k}} \left[M \frac{\partial \psi}{\partial x_{k}} \right] = 0, \tag{10}$$

$$R^{c} = \frac{\partial c}{\partial t} + u_{k} \frac{\partial c}{\partial x_{k}} - \frac{1}{1 + f^{\rho} c} \frac{\partial}{\partial x_{k}} \left[M \frac{\partial \psi}{\partial x_{k}} \right] = 0, \quad (11)$$

$$R_{i}^{u_{i}} = \rho \left[\frac{\partial u_{i}}{\partial t} + u_{k} \frac{\partial u_{i}}{\partial x_{k}} \right] + \frac{\partial}{\partial x_{k}} \left[p^{\text{eff}} \delta_{ik} - 2\mu^{\text{eff}} S_{ik} \right] - \rho g_{i}$$

$$- f_{i}^{\text{ST,CH}} + \frac{2}{3} \frac{\partial}{\partial x_{i}} \left[\mu \frac{f^{\rho}}{1 + f^{\rho} c} \frac{\partial}{\partial x_{k}} \left[M \frac{\partial \psi}{\partial x_{k}} \right] \right] = 0.$$
 (12)

Note that all governing equations are written in a residual form without further meaning. The unit coordinates and the strain rate tensor are denoted by the Kronecker Delta δ_{ik} and $S_{ik} = 0.5(\partial u_i/\partial x_k + \partial u_k/\partial x_i)$. The framework supports turbulent flows, where u_i corresponds to averaged or filtered velocities, and $p^{\text{eff}} = p + p^{\text{t}}$ is additionally augmented by a Turbulent Kinetic Energy (TKE, \hat{k}) term, i.e., $p^{\text{t}} = 2\rho\hat{k}/3$. Along with the Boussinesq hypothesis, the dynamic viscosity $\mu^{\text{eff}} = \mu + \mu^{\text{t}}$ of turbulent flows consists of a molecular and a turbulent contribution (μ^{t}), and the system is closed by a two-equation turbulence model to determine μ^{t} and \hat{k} in this study. The details of the turbulence modeling practice are outlined in Sec. II C. The term $f_i^{\text{ST,CH}}$ refers to the surface tension force of the CH approach, cf. (16) and details in Kühl, Hinze, and Rung, 25 which is replaced by a model in the present study.

Contributions arising from the two-phase CH model refer to the respective last terms of Eqs. (10)–(12) and the surface tension force in (12). The partial differential equations (PDEs) system agrees with the classical VoF framework for a vanishing mobility $M \to 0$. Moreover, an appreciated divergence-free velocity field (10) is obtained for $M \neq 0$ in combination with $f^{\rho} = 0$. Using the nonlinear material model $m^{(3)}$ in (8), f^{ρ} approximately vanishes due to $\partial m/\partial c \to 0$ virtually everywhere for sufficiently small values of $\gamma^{\rm m}$. While this yields the neglect of net diffusion fluxes in (10), it leaves a diffusive term within the concentration Eq. (11). The latter arises from the first part of the gradient of chemical potential ψ in Eq. (5). Such under-resolved CH–VoF methods consistently employ $f^{\rho} \to 0$ to simplify the PDE system, viz.,

$$R^{p} = \frac{\partial u_{k}}{\partial x_{k}} = 0, \tag{13}$$

$$R^{c} = \frac{\partial c}{\partial t} + \frac{\partial u_{k}c}{\partial x_{k}} - \frac{\partial}{\partial x_{k}} \left[\nu_{c} \frac{\partial c}{\partial x_{k}} \right] = 0, \tag{14}$$

$$R_{i}^{u_{i}} = \frac{\partial \rho u_{i}}{\partial t} + \frac{\partial u_{k} \rho u_{i}}{\partial x_{k}} + \frac{\partial}{\partial x_{k}} \left[p^{\text{eff}} \delta_{ik} - 2\mu^{\text{eff}} S_{ik} \right] - \rho g_{i} - f_{i}^{\text{ST,BR}} = 0.$$
(15)

Surface tension effects are now considered by the continuum model proposed by Brackbill, Kothe, and Zemach, 18 cf. Sec. II B 4. This is motivated when decomposing the surface tension force into an isotropic (pressure-like) term and a term proportional to C_2 , viz.,

$$f_{i}^{\text{ST,CH}} = \psi \frac{\partial c}{\partial x_{i}} = C_{1} \frac{\partial b}{\partial x_{i}} + \frac{C_{2}}{2} \frac{\partial}{\partial x_{i}} \left(\frac{\partial c}{\partial x_{k}}\right)^{2} - \frac{\partial}{\partial x_{k}} \left(C_{2} \frac{\partial c}{\partial x_{k}} \frac{\partial c}{\partial x_{i}}\right)$$
$$= \frac{\partial}{\partial x_{i}} p^{\text{ST,CH}} - \frac{\partial}{\partial x_{k}} \left(C_{2} \frac{\partial c}{\partial x_{k}} \frac{\partial c}{\partial x_{i}}\right). \tag{16}$$

The $p^{\rm ST,CH}$ -term scrambles with the pressure, and the second term is likely to vanish in under-resolved conditions due to $C_2 \sim \gamma_c$. The nonlinear apparent viscosity reads $\nu_c = M\partial^2 b/\partial c^2 = 2C_1\,M(6\,c^2-6\,c+1)$, cf. Sec. II B 1. It follows from a double-well potential $b=(c-1)^2c^2$ to be minimized in a phase separation process and locally acts either diffusive $(\nu_c \geq 0)$ or compressive $(\nu_c < 0)$. The two-phase flow model is closed by assigning the product C_1M to a spatially constant value that is guided by the numerical diffusion of the approximation for the convective concentration transport as suggested by Kühl, Hinze, and Rung. ²⁵

4. Surface tension for under-resolved flows

To consider surface tension effects in simulations that do not sufficiently resolve the thin interface, a model proposed by Brackbill, Kothe, and Zemach¹⁸ is used. The specific surface tension force reads

$$f_i^{\text{ST,BR}} = \sigma \kappa_\sigma \frac{\partial c}{\partial x_i},\tag{17}$$

where κ_{σ} denotes the curvature of the free surface, and the surface tension is assigned to the conventional value for air–water interfaces, i.e., $\sigma = 0.07 \, (\text{N/m})$ (at $T = 20 \,^{\circ}\text{C}$). The accurate calculation of the interface curvature is challenging for an interface-capturing approach. Therefore, the present study employs a suggestion of Ubbink, ³⁵ viz.,

$$\kappa_{\sigma} = -\frac{1}{V} \oint_{S(V)} \frac{\left(\frac{\partial \hat{c}}{\partial x_{i}}\right)}{\left|\frac{\partial \hat{c}}{\partial x_{i}}\right|} dS.$$
 (18)

Equation (18) is based on a smoothed concentration field \hat{c} , obtained from a Laplacian filtering operation that is repeated twice

$$\hat{c} = \mathscr{L}(\mathscr{L}(c)) \quad \text{with} \quad \mathscr{L}(c) = \frac{\sum_{f} c_f S_f}{\sum_{e} S_f}.$$
 (19)

Here, f indicates the faces of a control volume, and the face concentration values c_f are obtained from a simple linear interpolation of the adjacent cell centers.

C. Turbulence modeling

A hybrid filtered/averaging DES turbulence modeling approach is employed in the present study.³⁶ Among the various DES suggestions, we utilize the improved delayed detached eddy simulation (IDDES) model, which agrees with a frequently employed variant of Gritskevich *et al.*³⁷ and builds upon the popular shear stress transport (SST) \hat{k} - $\hat{\omega}$ Boussinesq viscosity approach of Menter, Kuntz, and Langtry.³⁸ To this end, the governing equations (13)–(15) are supplemented by two auxiliary equations to compute the required turbulent quantities, i.e., μ^{t} and $p^{\text{t}}(\hat{k})$, viz.,

$$R^{k} = \frac{\partial \rho \hat{k}}{\partial t} + \frac{\partial u_{k} \rho \hat{k}}{\partial x_{k}} - \frac{\partial}{\partial x_{k}} \left[\left(\mu + \sigma_{k} \mu^{t} \right) \frac{\partial \hat{k}}{\partial x_{k}} \right] - P^{k} + c_{\mu} \rho \hat{k}^{1.5} / L_{DES} = 0,$$
(20)

$$R^{\omega} = \frac{\partial \rho \hat{\omega}}{\partial t} + \frac{\partial u_k \rho \hat{\omega}}{\partial x_k} - \frac{\partial}{\partial x_k} \left[\left(\mu + \sigma_{\omega} \mu^{t} \right) \frac{\partial \hat{\omega}}{\partial x_k} \right] - \alpha \frac{\hat{\omega}}{\hat{k}} P^{k} + \beta \rho \hat{\omega}^{2} = 0.$$
 (21)

Here, $P^k = \mu^t S_{ik} S_{ik}$ represents the production of TKE, $\hat{\omega}$ marks a specific energy dissipation rate, and $L_{\rm DES}$ refers to a dissipation-related turbulent length scale. The Boussinesq viscosity concept is utilized to close the unresolved turbulent stresses $\rho u'_i u'_k$

$$\rho \overline{u'_i u'_k} = \rho \frac{2\hat{k}}{3} \delta_{ik} - 2\mu^t S_{ik}, \quad \text{with} \quad \mu^t = \rho \frac{\hat{k}}{\hat{\omega}} \frac{1}{\max[1, F_2|S_{ik}|/(\hat{\omega}a_1)]}.$$
(22)

The modeling coefficients α , β as well as σ_k and σ_ω are composed of an inner (1) and an outer (2) value, i.e.,

$$\varphi = F_1 \varphi_1 + (1 - F_1) \varphi_2. \tag{23}$$

The terminology distinguishes between classical inner and outer wall boundary layer regimes, where $\varphi_{1[2]}$ represents a constant inner (outer) coefficient value, and F_1 as well as F_2 correspond to blending functions of the background SST \hat{k} - $\hat{\omega}$ model.

The non-zonal transition from the filtered (LES) to the Reynolds averaged (RANS) approach is primarily managed by introducing the turbulent length scale $L_{\rm DES}$ in Eq. (20). The latter blends a grid-independent RANS definition $L_{\rm RANS} \sim \sqrt{\hat{k}/\hat{\omega}}$ —that varies in space and times—with a grid-dependent filter $L_{\rm LES} \sim \Delta$, viz.,

$$L_{\rm DES} = \hat{F}_{\rm d}(1+F_{\rm e})L_{\rm RANS} + (1-\hat{F}_{\rm d})L_{\rm LES}, \quad {\rm with} \quad L_{\rm LES} = c_{\rm DES}\Delta_{\rm mod}.$$
 (24)

The definition of the modified filter width Δ_{mod} employs the maximal edge length Δ of a control volume as well as the wall-normal distance d, viz.,

$$\Delta_{\text{mod}} = \min[c_{\text{w}} \max[d, \Delta], \Delta], \text{ with } \Delta = \max[\Delta_{x_1}, \Delta_{x_2}, \Delta_{x_3}]$$
(25)

with $c_{\rm w}$ being an empirical constant. An overview of the employed coefficients and blending functions is provided in Appendix A. In addition to Eq. (25), the blending functions $F_1, F_2, \hat{F}_{\rm d}$, and $F_{\rm e}$ also make intensive use of the wall-normal distance d. The definition of wall-normal distance is replaced by the instantaneous distance from the free surface, which is dynamically evaluated in a HPC-capable manner, cf. Sec. II D. Moreover, a sensor is used to indicate the operating mode of the turbulence closure at a given location, i.e., RANS ($\Omega_{\rm LES}=0$) or LES ($\Omega_{\rm LES}=1$), viz.,

$$\Omega_{\rm LES} = 1 - \frac{L_{\rm DES} - L_{\rm LES}}{L_{\rm RANS} - L_{\rm LES}}.$$
 (26)

D. Free surface distance

The turbulence closure requires the distance to the nearest airsea interface. The respective distance field is computed from the FV approximation of a Poisson equation with zero Dirichlet (Neumann) conditions along the free surface S_s (far-field $\partial \Lambda$) for a property \hat{d} (m²), viz.,

$$\frac{\partial^2 \hat{d}}{\partial x_k^2} = -1 \text{ in } \Lambda \text{ with } \hat{d} = 0 \text{ on } S_s \text{ and } \frac{\partial \hat{d}}{\partial x_k} = 0 \text{ on } \partial \Lambda,$$
(27)

as suggested by Tucker.³⁹ Since the free surface S_s , and therefore the location of boundary conditions, is grid embedded in the current approach, we manipulate the discrete equation system, cf. Eq. (2), near the free surface to secure zero values along the free surface, i.e.,

$$A^{\hat{d},P} = \alpha_{\hat{d}}$$
 and $\mathscr{S}^{\hat{d},P} = \beta_{\hat{d}}$. (28)

Here, $A^{\hat{d},P}$ and $\mathscr{S}^{\hat{d},P}$ refer to the main diagonal and the right-hand side of the algebraic equation system at a free surface cell. The identification of free surface cells to be manipulated is assigned to the concentration value c=0.5. The procedure tracks sign changes of (c-0.5) across the faces of the control volumes and applies the manipulation (28) to face adjacent cells. The parameter $\alpha_{\hat{d}}$ is assigned to a large number, e.g., $\alpha_{\hat{d}}=10^8$, whereas $\beta_{\hat{d}}$ depends on the concentration values of the face adjacent control volumes (1,2), viz.,

$$\beta_{\hat{d},j} = 2\alpha_{\hat{d}} \frac{|c_j - 0.5|}{|c_1 - c_2|} \quad \text{with} \quad j \in [1, 2].$$
 (29)

In line with Tucker³⁹ and Belyaev and Fayolle,⁴⁰ the finally employed free surface distance field d (m) follows from

$$d = \sqrt{\frac{\partial \hat{d}}{\partial x_k} \frac{\partial \hat{d}}{\partial x_k} + 2\hat{d}} - \left| \frac{\partial \hat{d}}{\partial x_k} \right|. \tag{30}$$

E. Wind-wave tank

Applications included in Sec. V refer to wind–wave flume experiments of Buckley and Veron, $^{41-43}$ which were obtained in a flume that approximately spans 42 (length x_1) × 1 (width x_2) × 1.25 m³ (height x_3). An upstream blower initiated the experimental waves to the free surface. The waves subsequently develop under strong wind forcing toward the study area of the experimental data, located approximately 23 m downstream of the airflow input. Experimental data are characterized by phase-averaged mean velocities in the air phase and wave parameters, representing the characteristics of the experimental wave train at its peak frequency, cf. Table I. Measured results mainly refer to

two-component particle image velocimetry (PIV) data and their post-processing.

The numerical wind–wave tank spans only a smaller section of the experimental flume to support the feasibility of the simulations. The considered domain is sized by the primary wavelength reported in the experiments, cf. Table I. The horizontal (x_1) extent covers 11 wavelengths λ and extends up to 6 m for the larger investigated wavelength. The vertical (x_3) extension of 2.3 λ agrees with the experimental flume (1.25 m) for the larger investigated wavelength, of which 1.3 λ (0.7 m) is water wetted in still-water conditions. The lateral (spanwise, x_2) extent refers to 0.4 λ , i.e., 22% of the experimental width for the larger wavelength.

Figure 1 illustrates the grid setup in the x_1 – x_3 -plane. The box-type computational domain comprises four zones, an inlet and forcing zone (λ) at the upstream end (cf. Sec. II E 2), followed by a wave development zone (2λ), a centrally located study area (4λ)—where results are extracted and compared with experiments—and a beach zone (4λ) to suppress wave reflections from the downstream located outlet. The grid consists of hexahedral control volumes refined around the free surface. The vertical refinement reaches a maximum resolution of $1.4 \times 10^{-3} \lambda$. The grid is substantially stretched horizontally toward the outlet in the beach zone to ensure adequate wave damping. The most crucial aspect for the comparability of experimental and numerical results is the formulation of appropriate inlet or approach flow conditions for momentum, turbulence, and surface elevation conditions (concentration) upstream of the study area described in Secs. II E 1 and II E 2.

1. Approaching air-phase flow

The inlet conditions and the near-inlet forcing of the air velocities are space and time-dependent, and support considering transient, propagating orbital motion contributions to the specification of the air-phase velocity. Due to the lack of detailed scale-resolving experimental data upstream of the study area, a simple logarithmic profile based on the experimentally observed mean turbulent velocity \bar{u} is adopted, cf. Sec. III B. In essence, detailed turbulent structures are suppressed by the considered inlet conditions, and only the dynamic mean data are imposed. The horizontal velocity profile of the air phase $u_1^{\rm air}$, therefore, involves the superposition of two contributions: a smaller orbital motion contribution $u_1^{\rm orb,air}$, that is continuous across the air–sea interface and detailed in Sec. IIE2, in addition to a

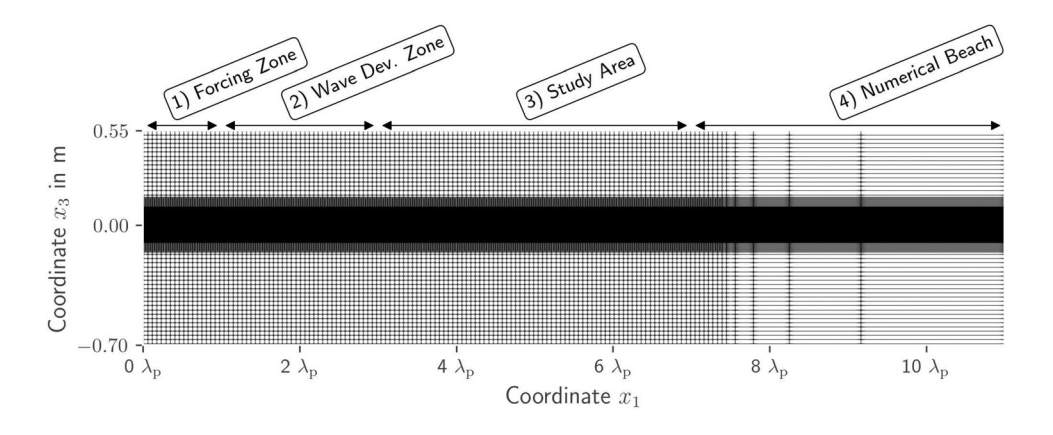


FIG. 1. Illustration of the x_1 – x_3 -plane of the computational domain. The calm water free surface is located at $x_3=0$ and waves travel horizontally in the positive x_1 -direction underneath a similarly directed air stream. The domain is subdivided into a forcing zone (1), a wave development zone (2), a study area (3), and a numerical beach (4). For an exemplary resolution of $\Delta_{(x_1,x_2,x_3)}^{min} = [2.8,2.8,1.4] \times 10^{-3} \lambda_p$, the grid consists of 31.7×10^6 control volumes.

horizontal logarithmic mean air-phase velocity profile $\bar{u}_1^{
m air}$. Accordingly, this results in

$$u_1^{\text{air}} = \bar{u}_1^{\text{air}} + u_1^{\text{orb,air}}$$

with

$$\bar{u}_{1}^{air} = \frac{u_{*}}{\kappa} \ln \left(\frac{d+z_{0}}{z_{0}} \right) c_{in} , \quad u_{2}^{air} = 0 , \quad u_{3}^{air} = u_{3}^{orb,air}.$$
 (31)

Here, κ , u_* , d, and z_0 refer to the Von-Karman constant, the friction velocity, the distance normal to the free surface and a roughness length. All mean-flow parameters were chosen according to the data described by Buckley and Veron. Moreover, a bulk-correction coefficient $c_{\rm in}$ is introduced to conserve a time-invariant entering airvolume flux. The air-phase velocity is dynamically imposed above the wave in a forcing zone extending one wavelength downstream from the inlet by using the implicit forcing approach described in Sec. II E 2. Mind that the forcing is applied to all velocity components (even if their value is zero).

2. Approaching water-phase flow and implicit forcing

Two water-phase-based challenges need to be addressed by the numerical wave tank, i.e., controlling the wave propagation toward the study area and suppressing upstream traveling disturbances from the outlet into the study area. Waves generation and propagation are often simulated with numerically efficient inviscid methods. More complex phenomena, such as strong wind forcing or breaking waves, require considering viscous, turbulent, and potentially two-phase flow effects. However, scale-resolving large-domain turbulent flow simulations are afflicted with prohibitive spatiotemporal resolution requirements for an accurate propagation of the incident flow toward the study area. Accordingly, small spatial domains are desirable to reduce computational effort when periodic conditions are arguably debatable for complex flow problems. Periodic boundary conditions force wave trains to adjust to a constant wavelength, which may not correspond to the true nature of a growing wind wave and could therefore cause unfavorable disturbances, especially when the flow becomes more complex (e.g., breaking waves).

Coupled viscous/inviscid methods are an attractive way out of the dilemma mentioned above. In particular, a one-way coupling between an inviscid baseline solution and the viscous solution can facilitate an efficient way for air-sea interface simulations at a moderate computational cost. In line with Wöckner, Drazyk, and Rung⁴ and Luo-Theilen and Rung, 45,46 an appealing one-way coupling refers to an implicit solution forcing. The approach essentially manipulates the algebraic equation system to comply with a prescribed solution obtained from either nonlinear or linear wave theories for the velocity and concentration at the inlet boundaries. The manipulation of the flow is gradually relaxed toward the interior in a forcing zone that extends approximately one wavelength, cf. Fig. 1. The present study also applies the forcing strategy to the air phase to impose the conditions described in Sec. II E 1. Dirichlet conditions naturally supplement the approach along the inlet plane, cf. Sec. II E 3. The implicit forcing is based on an appropriate manipulation of the coefficient matrix resulting from the FV discretization of the governing Eqs. (14) and (15) and proves to be very robust. The manipulation follows the suggestion outlined in Eq. (28) and reads

$$A^{\varphi,P} \to (1 + \beta_s \alpha_s) A^{\varphi,P}$$
 and $\mathscr{S}^{\varphi,P} \to \mathscr{S}^{\varphi,P} + (A^{\varphi,P} \beta_s \alpha_s) \varphi^P$, (32)

where φ and φ^P refer to the manipulated variable and its prescribed inviscid solution at the discrete location P. The non-dimensional relative magnitude β_s controls the forcing intensity. As outlined by Wöckner, Drazyk, and Rung, ⁴⁴ small values of β_s are sufficient due to forcing a larger region, i.e., $\beta_s = 10^{-2}$ in the present study. The scalar shape function α_s controls the spatial extent of the forcing, and the present study employs a quadratic drop from unity to zero over one wavelength with increasing distance from the inlet boundary, cf. Fig. 1.

Using the above-described forcing, any (known) wave-wind condition, i.e., any prescribed φ^P in Eq. (32), can be superposed to mimic the experimental conditions. The present study employs simple (monochromatic) 2D (plane) Airy waves, which rapidly expose nonlinear features while propagating through the wave development zone and make applying non-linear wave prescriptions seem unnecessary. As an example, the following applies to the orbital velocities $u_i^{\rm orb}$ of the air, and the sea phase employed herein, viz.,

$$u_{1}^{\text{orb,sea}} = a_{p}\omega_{p}\cos(\omega_{p}t - k_{p}x)e^{-kd}, \quad u_{2}^{\text{orb,sea}} = 0, u_{3}^{\text{orb,sea}} = -a_{p}\omega_{p}\sin(\omega_{p}t - k_{p}x)e^{-kd},$$
(33)

and

$$u_1^{\text{orb,air}} = -a_p \omega_p \cos(\omega_p t - k_p x) e^{-kd}, \quad u_2^{\text{orb,air}} = 0, u_3^{\text{orb,air}} = -a_p \omega_p \sin(\omega_p t - k_p x) e^{-kd},$$
(34)

where d again refers to the free surface distance provided by Eq. (30), $k_{\rm p}$ refers to the wave number, and the subscript p denotes the peak frequency. The imposed wave parameters are assigned to experimentally reported values for the wave amplitude $a_{\rm p}$, wavelength $\lambda_{\rm p}$, and its frequency $\omega_{\rm p}=2\pi f_{\rm p}$. Lateral velocities are again suppressed. Figure 2 compares measured and computed wave spectra upstream of the study area.

3. Other boundaries

A second challenge refers to the behavior of the wave field down-stream of the study area. Successive wave reflections from the far-field boundaries might restrict the exploitable part of transient simulations, particularly for short outlet distances. The suppression of such reflections requires significant numerical damping downstream of the study area. The latter is frequently achieved by the introduction of a damping zone ("numerical beach"), which is usually realized utilizing grid-stretching and/or diffusive approximations of the convective kinematics in Eq. (14). This aims at damping the waves before they reach the outlet boundary and can be combined with a simple hydrostatic pressure outlet in calm water conditions.

Other boundary conditions can be taken from Table II. As mentioned in Sec. II E 2, the forcing approach is supplemented by Dirichlet conditions at the inlet (x_1^{\min}) for the velocity u_i and the concentration field c. The pressure p follows from Neumann boundary conditions. At the outlet (x_1^{\max}) , a simple hydrostatic pressure profile is used, with Neumann conditions for the velocity and the concentration field. At the lateral and vertical boundaries, zero Neumann conditions are applied for all quantities.

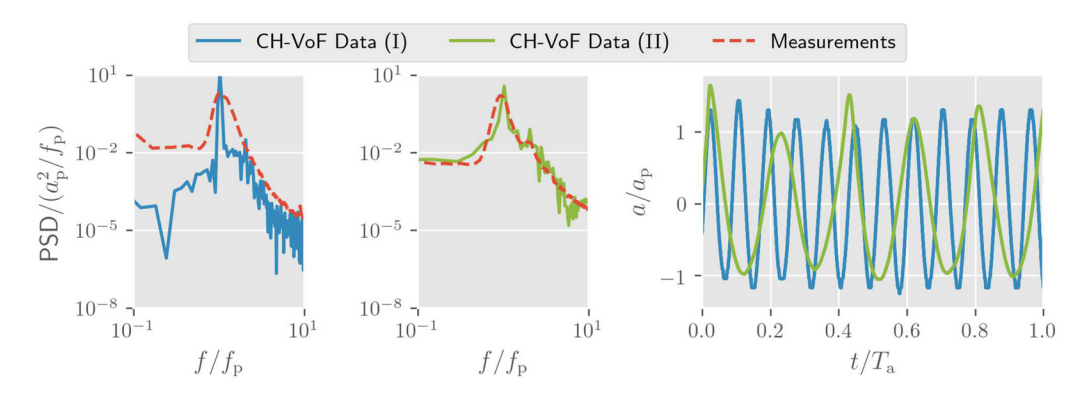


FIG. 2. Normalized power spectral densities (PSDs) of waves approaching the study area for a low (scenario I; left) and a high wind speed case (scenario II; center), supplemented by the corresponding time series of the simulation data (right). Comparison of present simulations (green, blue) with measured data (red) of Buckley and Veron. All data normalized with inlet wave parameters, cf. Table I. Reproduced with permission from Buckley and Veron, J. Phys. Oceanogr. 46, 1377–1397 (2016). Copyright 2016 American Meteorological Society.

III. DATA ACQUISITION AND DATA ANALYSIS

The data analysis and data acquisition strategy employs phase-averaged, wave-following coordinates, which supports the comparison with the experimental data. The procedure is briefly described below. A more comprehensive discussion can be found in Hara and Sullivan⁴⁷ or Buckley and Veron.⁴¹

A. Analytic signal

The data analysis is based on the phase information of each cell within the spatiotemporal domain. The phase information is retrieved from the analytic signal η_a of the smoothed wave elevation field $\hat{\eta}$. A Hilbert transformation $\mathcal{H}(\hat{\eta})$ is used to calculate this analytic signal by zeroing out the negative frequency components, turning the real-valued signal into a complex-valued signal

$$\eta_{\mathbf{a}} = \mathscr{F}^{-1}(\mathscr{F}(\hat{\eta})2\theta) = \hat{\eta} + i\mathscr{H}(\hat{\eta}). \tag{35}$$

In Eq. (35), \mathscr{F} corresponds to the Fourier Transformation and θ to the Heaviside step function. The phase information is simply derived from the imaginary part of η_a , viz.,

$$\phi = \mathfrak{Jm}(\eta_a),\tag{36}$$

and is used to perform the decomposition of the flow quantities as outlined in Sec. III B. An individual smoothed wave elevation field $\hat{\eta}$ is determined for each (post-processed) time instant. For this purpose, the horizontal calm-water (x_1-x_2) plane is discretized employing a regular 2D meta-grid in the study area region. The extensions of this meta-grid, its centroid positions, and edge lengths do not need to agree

TABLE II. Summary of the applied boundary conditions.

	x_1^{\min}	x_1^{\max}	$x_2^{\min,\max}$	$x_3^{\min,\max}$
u_i	Dirichlet	Zero grad.	Zero grad.	Zero grad.
P	Zero grad.	Hydro. pressure	Zero grad.	Zero grad.
С	Dirichlet	Zero grad.	Zero grad.	Zero grad.
$\hat{k},\hat{\omega}$	Dirichlet	Zero grad.	Zero grad.	Zero grad.

with the corresponding plane of the CFD grid, though this is virtually true in the present study. First, each CFD control volume in the study area is associated with a particular cell of the meta-grid. Subsequently, the vertical (x_3 -) coordinate for all control volume centroids of the study area that satisfy $d < 2\Delta_{x_3}$ is registered at their associated meta-grid cell, where the factor of two is used to avoid empty meta-grid cells. The calculated free surface elevation of a meta-grid cell refers to an average of the registered vertical coordinates in the case of multiple entries. Finally, the resulting elevation field is smoothed, using a Laplacian filtering operation—similar to Eq. (19).

B. Triple decomposition

The flow field is not analyzed by reference to the Cartesian coordinates (x_1, x_2, x_3) but as a function of the wave following coordinates ζ and ϕ . The vertical coordinate ζ is assigned to the distance field d, also employed by the turbulence closure model, cf. Sec. II C. Furthermore, the phase information of each cell follows from the Hilbert transformation of the wave elevation field (36), described in Sec. III A. Following the well-known Reynolds decomposition, the instantaneous velocity field $u_i(\phi,\zeta)$ can be decomposed into a mean velocity $\langle u_i \rangle (\phi,\zeta)$ and a turbulent fluctuation $u_i'(\phi,\zeta)$, viz.,

$$u_i(\phi,\zeta) = \langle u_i \rangle (\phi,\zeta) + u_i'(\phi,\zeta). \tag{37}$$

When considering the interaction between air and sea, it is helpful to use a triple decomposition introduced by Phillips.²⁷ The triple decomposition fractions the mean $\langle u_i \rangle$ into an ensemble mean $\bar{u}_i(\zeta)$ over all phases (between $-\pi$ and π) and a wave-coherent component $\tilde{u}_i(\phi, \zeta)$. The instantaneous velocity $u_i(\phi, \zeta)$ thereby follows from

$$u_i(\phi,\zeta) = \bar{u}_i(\zeta) + \tilde{u}_i(\phi,\zeta) + u'_i(\phi,\zeta). \tag{38}$$

The triple decomposition can also be applied to other primitive variables, e.g., the pressure *p*.

IV. VERIFICATION AND VALIDATION

The diffusive interface model and its implementation have been validated for capillary and gravity-driven two-phase flows in a previous publication by the authors. ²⁵ To verify the free surface distance calculation outlined in Sec. II C and the data processing described in

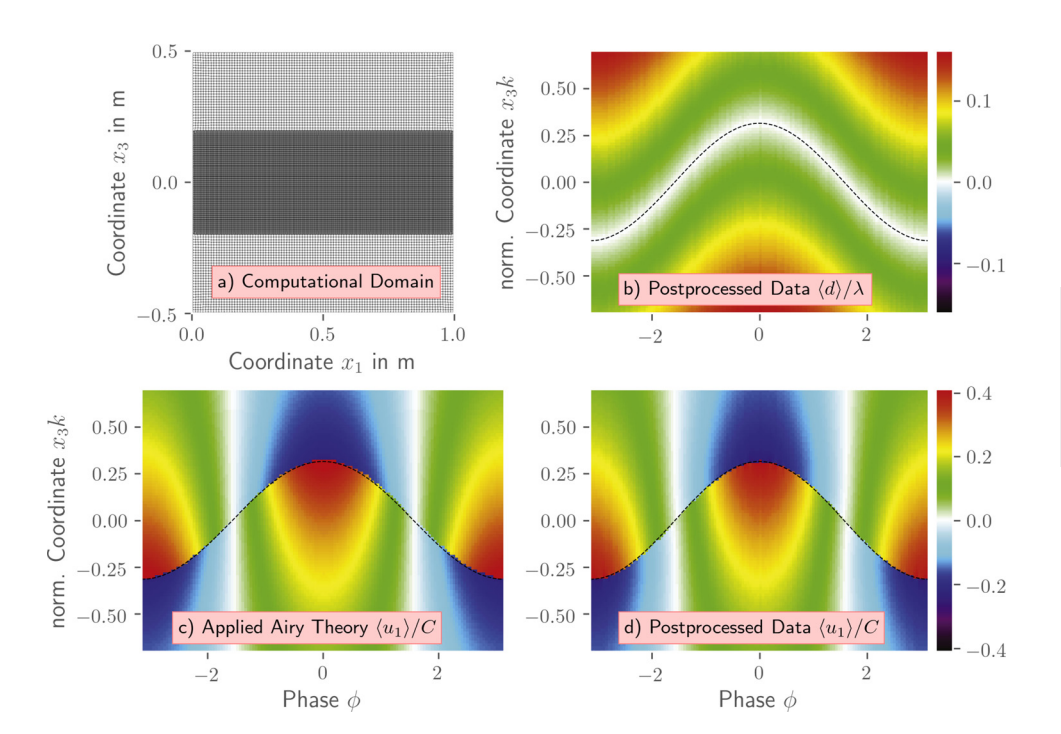


FIG. 3. Results obtained for the verification case: (a) computational domain, (b) normalized post-processed distance field $\langle d \rangle / \lambda$, as well as a comparison of the prescribed (c) and processed (d) normalized velocity $\langle u_1 \rangle / C$ —including an indication of the free surface by dashed lines.

Sec. III, we analyze a simple moving wave test case in a two-dimensional domain (Fig. 3).

The velocity and concentration fields are prescribed in the entire domain by the linear wave theory using the boundary conditions described in Secs. II E 1 and II E 2. The size of the domain reads $\lambda \times \lambda$, using a unit wavelength $\lambda=1$ m and a wave amplitude of a=0.1 λ . Wave number k and phase velocity C are defined as $k=2\pi/\lambda$ and $C=\lambda f$, with f representing the frequency of the linear wave. The calm-water surface is assigned to the central height $(x_3=0)$. The domain is uniformly discretized in the upper and lower regimes using $\Delta_{x_1}=\Delta_{x_3}=0.01$ λ . To ensure a sufficient post-processing resolution, a refined grid with $\Delta_{x_1}=0.005$ λ , $\Delta_{x_3}=0.0025$ λ is employed near the free surface.

The results of the verification test are shown in Fig. 3. The processed mean velocity $\langle u_1 \rangle / C$ displays a good agreement with the prescribed data. The average distance field $\langle d \rangle / \lambda$ also offers a reasonable distribution. Minor differences result from the simplified representation of x_3k in the post-processed data, which becomes apparent by a slightly different distribution of the velocity close to the surface in both the air and the water. Instead of a more complex coordinate transformation, ^{42,48} the field data are shifted in the vertical direction only. This simplified transformation is similar to the approach used by Funke *et al.*⁴⁹ and Husain *et al.*⁷ and reduces the complexity of the post-processing routine.

V. APPLICATION

In this study, two well known wind–wave scenarios (I and II) with realistic Reynolds numbers up to $Re_{\lambda}\approx 20\,000$ are computed. Both scenarios are based on a previous experimental investigation reported in Buckley and Veron, where the air–sea interface is subject to strongly forced conditions. The experimentally reported results refer to airflow velocities obtained from particle-image-velocimetry (PIV) measurements. They have recently been supplemented by pressure data

compiled from the measured velocities of the first (I) and a slightly different third (III) scenario. ⁴⁹ Mind that the third scenario (III) was not directly simulated but is used for comparisons of the pressure fields in Sec. V C, because it shows similar flow phenomena to scenario II while the wave slopes and wave ages are of comparable magnitude.

The experimentally investigated wind–wave spectra were narrow-banded, with clear peaks at a dominant wave frequency f_p . The tabulated data are used to derive the inlet conditions for the air and the sea phase as outlined in Sec. II E 2 and characterizes the wave fields solely with the help of the identified peak frequency f_p . The study focuses on young waves, frequently labeled wind–waves, where the phase velocity C_p is of a similar order of magnitude as the friction velocity u_* along the air–sea interface. Accordingly, this study's wave age parameter C_p/u_* is relatively small, cf. the classification suggested by Belcher and Hunt 50 ($C_p/u_* < 10$). Other characteristic parameters used in the study are also outlined in Table I.

The material properties of the air (water) phase were set at a density ρ of 1 kg/m³ (10³ kg/m³) and at a dynamic viscosity μ of 17 \times 10⁻⁶ Pa s (10⁻³ Pa s). The CH–VoF parameter C_1M of the apparent viscosity ν_c is given by a temporal and spatially constant value mentioned in Table III. The latter follows precursor studies on the numerical diffusion of the convective concentration transport, as outlined by Kühl, Hinze, and Rung. Due to the larger interface curvature radius of the first scenario (I), surface tension forces are only considered for the second scenario (II), where narrow wave crests occur. To this end, the surface tension force σ and gravitational acceleration g are set to 0.07 N/m and 9.81 m/s², respectively.

The investigated domain, grid setup, and boundary conditions are described in Sec. II D. For both scenarios, the grid features a resolution of $\Delta_{(x_1,x_2,x_3)}^{min} = [2.8,2.8,1.4]\times 10^{-3}\lambda_p$ at the interface resulting in 31.7×10^6 control volumes. A brief grid dependency study has demonstrated the adequacy of the resolution. Mind that the grid

TABLE III. Employed simulation parameters, i.e., apparent viscosity C_1M of the CH–VoF model (cf. Sec. IIB 1), surface tension σ , time step Δ_t , data averaging time T_{avg} , number of data-processing wave periods N_{avg} , and normalized grid spacings in the refinement zone.

Scenario	C_1M (m ² /s)	σ (N/m)	$\Delta_{t}\left(\mathbf{s}\right)$	T_{avg} (s)	$N_{ m avg}$	$\Delta_{(x_1,x_2)}/\lambda_p$	$\Delta_{x_3}/a_{ m p}$
I	5×10^{-5}		1×10^{-4}	3.5	11.5	2.8×10^{-3}	1.4×10^{-1}
II	1×10^{-3}	0.07	1×10^{-4}	3.0	5.6	2.8×10^{-3}	3.3×10^{-2}

is strongly stretched in the beach zone, so the final cell spacing satisfies $\Delta_{x_1} > \lambda_p$. Depending on the scenario, the resolution in the refinement zone leads to a wide coverage of the LES spectrum, from $y^+ \approx 2$ (close to DNS, scenario I, air phase) up to $y^+ \ge 200$ (scenario II, water phase). The high resolution in the first scenario is also due to the low slope, since the wave height should be resolved by a minimum number of cells to still accurately represent the surface. Constant time steps with $\Delta_t = 10^{-4}$ s are employed in both cases, which resolve the peak wave period by approximately 3000 (I) and more than 5000 (II) time steps. The complete simulations covered about 23 (I) and 15 (II) periods, including the initial transient phase and a subsequent data averaging time T_{avg} . The former is complete once the initial wave train has passed through the domain. During the subsequent 3.5×10^4 (I) and 3.0×10^4 (II) time steps within T_{avg} , 1 of 50 time steps is used for the averaging process. Accordingly, the data processing involves $N_{\text{avg}} = 11.5$ (I) and $N_{\text{avg}} = 5.6$ (II) wave periods.

Exemplary normalized power spectral densities (PSDs) and the corresponding time series of the waves—extracted upstream of the study area—are shown in Fig. 2. PSD data are based on each time step within $T_{\rm avg}$ and are evaluated using a basic Hann function. Compared with the measurement data in Buckley and Veron, the simulation results show a slightly narrower spectrum close the peak frequency while the general shape is in good agreement. However, the initially linear waves of the simulation quickly evolve into non-linear waves, with broader wave troughs and narrower crests. Note that this rough comparison of the spectra is only to ensure that the experimentally observed waves are comparable to the waves entering study area of our model. A longer evaluation period for the spectra was therefore not realized due to the computational effort and the already converged flow quantities.

Contour plots of instantaneous, wave coherent, and mean velocities, in addition to mean pressures and wave coherent shear stresses, serve to compare numerical and experimental data in the remainder of this section. Contours are displayed in the (x_1, x_3) -plane and computational data are compiled from lateral averages along the homogeneous x_2 -direction. In connection with the pressure field, drag and viscous stresses are estimated and compared with measurement data. Wave coherent quantities are calculated within the study area as a function of the wave following coordinates ζ and ϕ , cf. Sec. III B. Moreover, we compare similarly obtained contour plots for the (resolved and modeled) computed Reynolds stresses with measured turbulent stresses and investigate the averaged horizontal velocity profile $\bar{u}_1(\zeta)$ as well as averaged stresses along the vertical coordinate ζ . All data are normalized using the characteristic parameters, e.g., mentioned in Table I. Amplitudes of the simulated waves within the study area deviate only slightly from the prescribed peak values because they grow slowly as they propagate through the domain.

A. Instantaneous horizontal velocity and vorticity

A first qualitative comparison of experimental and computational results is provided in Fig. 4. Figure displays snap-shot values of the predicted (left) and measured (right) normalized instantaneous horizontal velocities u_1/u_{10} for both wave scenarios. The top sub-figures depict the first scenario, which refers to a low wind speed wave with a smaller slope $a_{\rm p}k_{\rm p}\leq 0.09$, and the bottom sub-figures display the second high wind speed scenario.

Displayed results reveal similar flow structures and velocity values, i.e., u_1 increases above the crests and decreases above the troughs. In line with experiments, low-velocity fluid is ejected away from the free surface along the downwind face of the waves for the scenario I. The orbital motion is seen in the water phase prediction, which—due to missing approach flow turbulence—displays only very subtle turbulence activity. As indicated in the bottom sub-figures, both simulation and experiment for the second scenario reveal significant instantaneous airflow separation behind the crest. The waves of the second, much steeper ($a_{\rm p}k_{\rm p} \geq 0.27$), scenario expose substantial non-linear features.

Moreover, the vorticity $\omega_2 = \partial u_1/\partial x_3 - \partial u_3/\partial x_1$ in the sheltered (leeward) layer of the second scenario is relatively uncorrelated, featuring islands of low vorticity, which was also reported in the experiments as an indicator for substantial airflow separation (Fig. 5).

B. Wave-coherent velocities and shear stress

To assess the influence of different wind-wave conditions on the mechanical energy fluxes along the air-sea interface, it is convenient to analyze the wave-coherent flow quantities that result from the triple decomposition introduced in Sec. III B with Eq. (38).

Figure 6 depicts contour plots of the horizontal wave coherent velocity \tilde{u}_1 for both scenarios, which were analogously extracted from the experimental and computational data. Experimental data are displayed in the right graphs of the top and center rows, while all other sub-figures refer to computational results. Orbital motion patterns can be observed below the free surface in both scenarios. Experiments (PIV) and simulations (CH-VoF) agree that in both cases, the effect of waves is to accelerate the horizontal airflow along the upstream face of the wave and decelerate the airflow along the downstream face. For the low wind speed scenario (I, top), the experimental and numerical results for \tilde{u}_1 are in acceptable agreement. In contrast to the experimental data, the areas of extreme velocities are larger and more pronounced in the simulation results. In this regard, the agreement between numerical and experimental data improves significantly for the high wind speed scenario (II, center). For the high wind speed case (II) displayed in the center of Fig. 6, the orbital motions of the air phase are hardly perceptible. On the contrary, the orbital motions clearly transit from the sea phase into the lower part of the air phase for the low wind speed case (I) displayed in the top sub-figures.

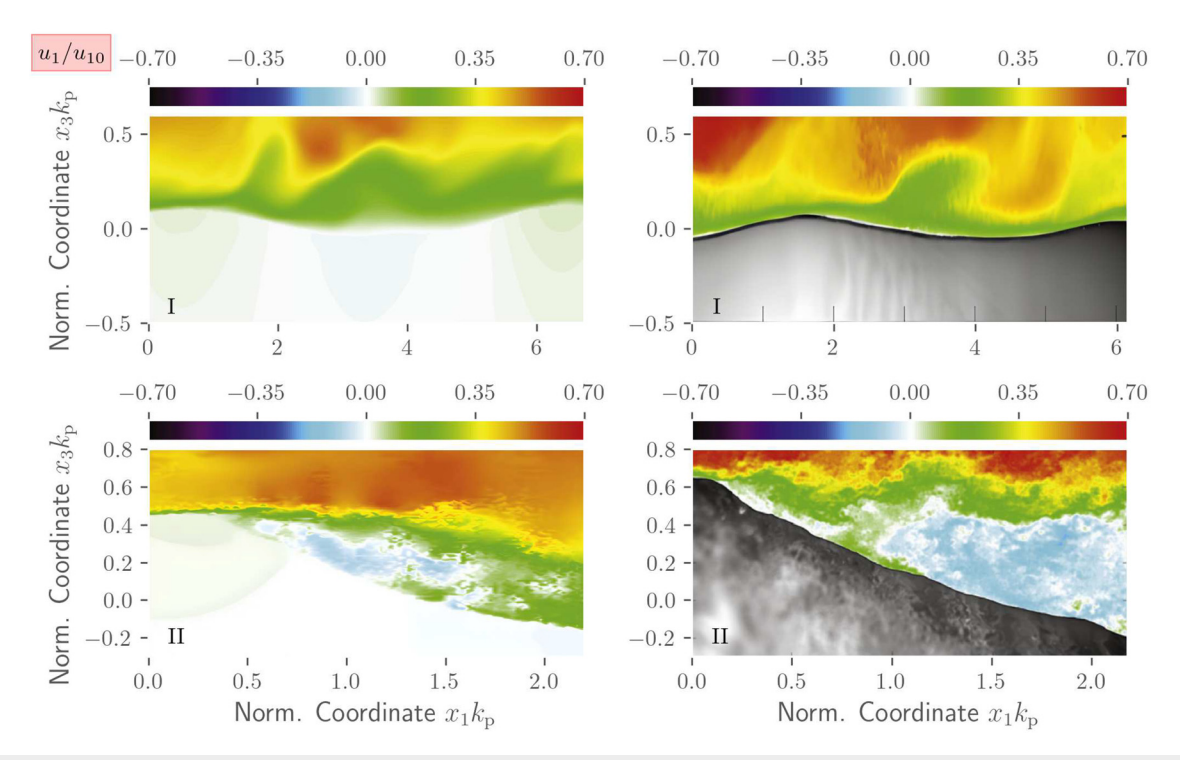


FIG. 4. Comparison of (laterally- Ix_2 -averaged) instantaneous normalized horizontal velocity fields u_1/u_{10} in the study area reported from the present simulations (left) and the experiments of Buckley and Veron³³ (right) for a low (scenario I; top) and a high wind speed wave (scenario II; bottom). Reproduced with permission from Buckley and Veron, Eur. J. Mech.-B/Fluids **73**, 132–143 (2019). Copyright 2019 Elsevier B.V.

Having entered the air phase regime in case I, the \tilde{u}_1 -contours indicate a pronounced shift in the negative phase direction before turning into the positive direction above the critical layer $x_3 \geq x_3^{\rm crit}$. The latter is defined by $\langle u(x_3^{\rm crit})\rangle = C_{\rm p}$ and is indicated by the dashed gray line in each sub-figure. As confirmed by the experiments, the height of the simulated critical layer drastically increases with increasing wave age (Fig. 6). The height of the critical layer is larger above the downstream face than above the upstream face of the wave, which again outlines the accelerating/decelerating effect of the waves along the upstream/

downstream face, respectively. This asymmetry reduces when increasing the wave age. For the high wind speed wave, the critical layer is fairly thin, i.e., $x_3k_{\rm p}^{\rm max}\approx 0.02$, and thus hardly perceptible. By reference to Figs. 6–8, it is seen that the critical layer is generally thinner in the experiment than in the simulation. This is due to a slightly different air-phase boundary layer above the wavy interface in the simulations, which is further discussed in Sec. V C. Furthermore, a positive phase shift of approximately $\pi/3$ against the wave pattern is observed for the critical layer in both simulations and experiments.

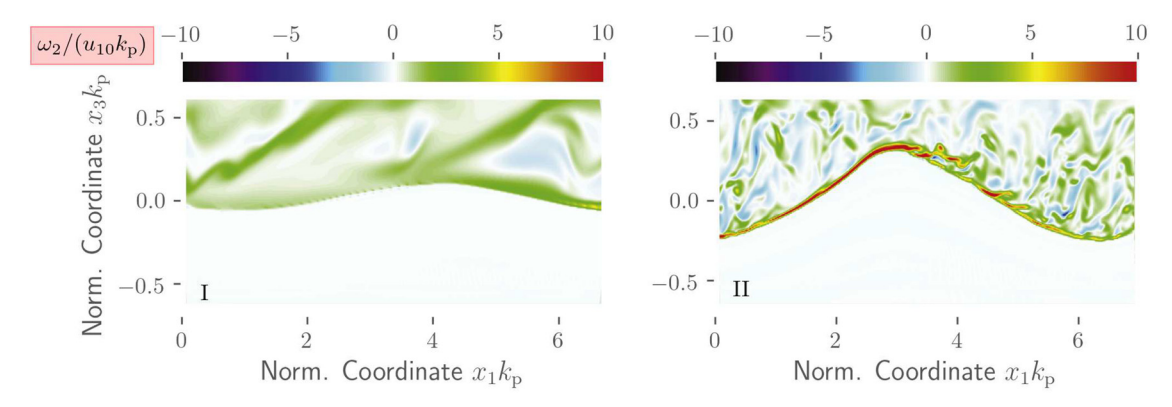


FIG. 5. Comparison of instantaneous normalized vorticity fields $\omega_2/(u_{10}k_p)$ in the study area reported from the present simulations for a low (scenario I; left) and a high wind speed wave (scenario II; right).

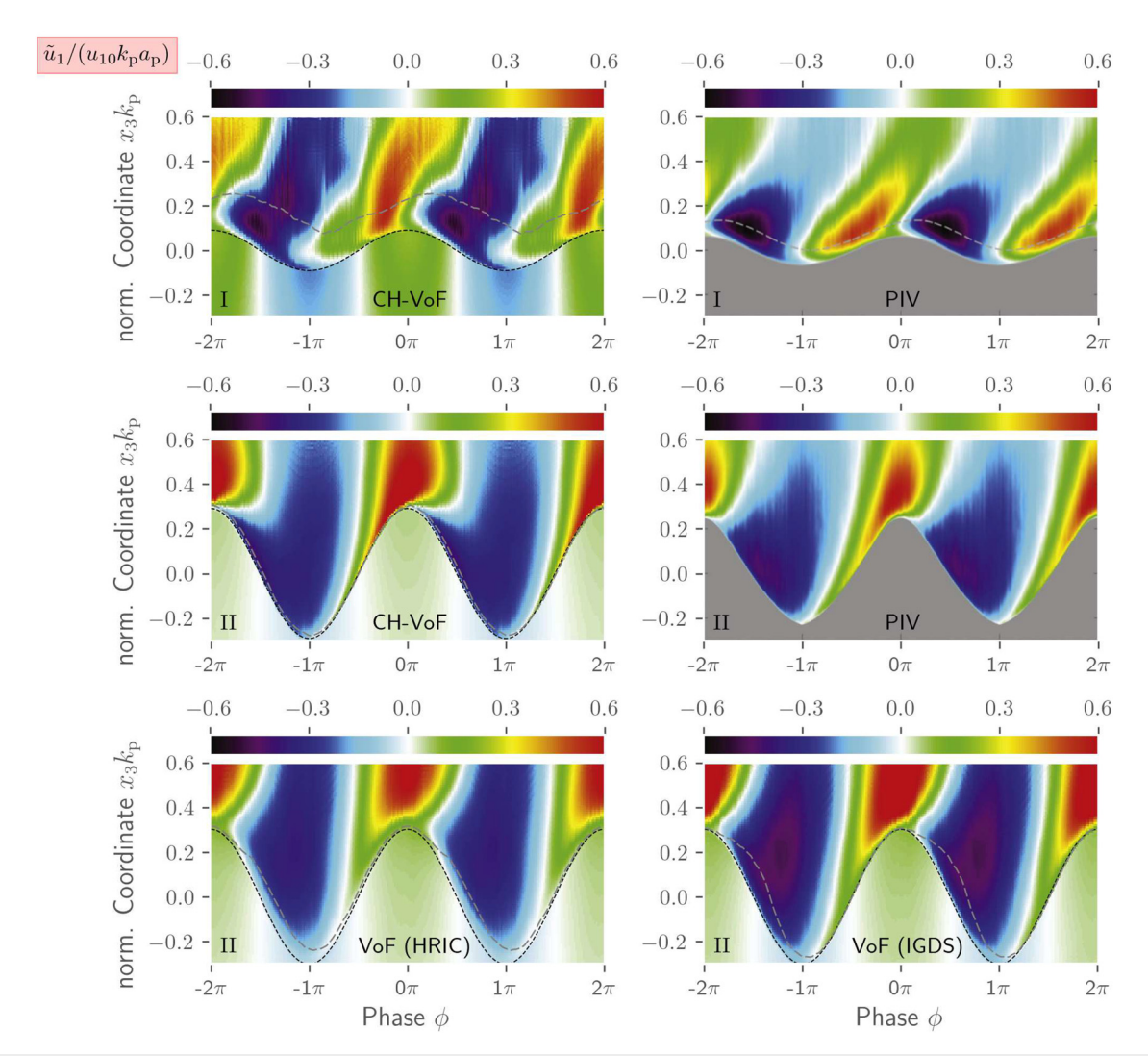


FIG. 6. Comparison of (laterally averaged) normalized horizontal wave-coherent velocity fields $\tilde{u}_1/(u_{10}k_pa_p)$ as a function of vertical coordinate x_3k_p and the phase position ϕ . Top and center row: The results obtained from the present simulations (CH–VoF, left) and the experiments of Buckley and Veron⁴³ (PIV; right) for a low (scenario I; top) and a high wind speed wave (scenario II; center). Bottom row: Supplementary results obtained from classical VoF simulations using different convective approximations: HRIC (left) and IGDS (right). Dashed gray line indicates the height of the critical layer. Coloring is restricted to the measurement data, which is partly only available as images. For illustration, an alternative coloring is used in Appendix B. Reproduced with permission from Buckley and Veron, Eur. J. Mech.-B/Fluids **73**, 132–143 (2019). Copyright 2019 Elsevier

Above the critical layer, the behavior of the velocities \tilde{u}_1 and \tilde{u}_3 changes due to the increasing influence of the applied wind forcing. Figure 6 indicates that \tilde{u}_1 follows an alternating pattern along the top of the study area, which is phase-aligned with the wave pattern for both investigated scenarios. When approaching the critical layer from above in Fig. 6, a phase lag is observed in both the experimental and numerical data, as indicated by the shape of the white contour lines. The maximum upstream lag of the horizontal velocity reaches approximately $\pi/3$ in the upper portion of the critical layer for the old wave case (I). Subsequently, it reduces toward zero along the interface. In line with the experimental observation, a different picture emerges for the high wind speed case (II), where the upstream phase lag

continuously increases toward $\pi/2$ when approaching the free surface from above, cf. the center row of Fig. 6. For both scenarios, simulations and experiments reveal the dominance of upstream directed motion \tilde{u}_1 in the trough region.

Similar observations can be made for the vertical velocity component \tilde{u}_3 , depicted in Fig. 7. The influence of the more pronounced critical layer is again obvious in the first scenario, where the orbital motion transits through the free surface into the air phase. When entering the critical layer from below, the contour lines of the vertical velocity bend sharply in the upstream direction between the free surface and the upper boundary of the critical layer. Above the critical layer, the situation changes, and the contour lines remain at an

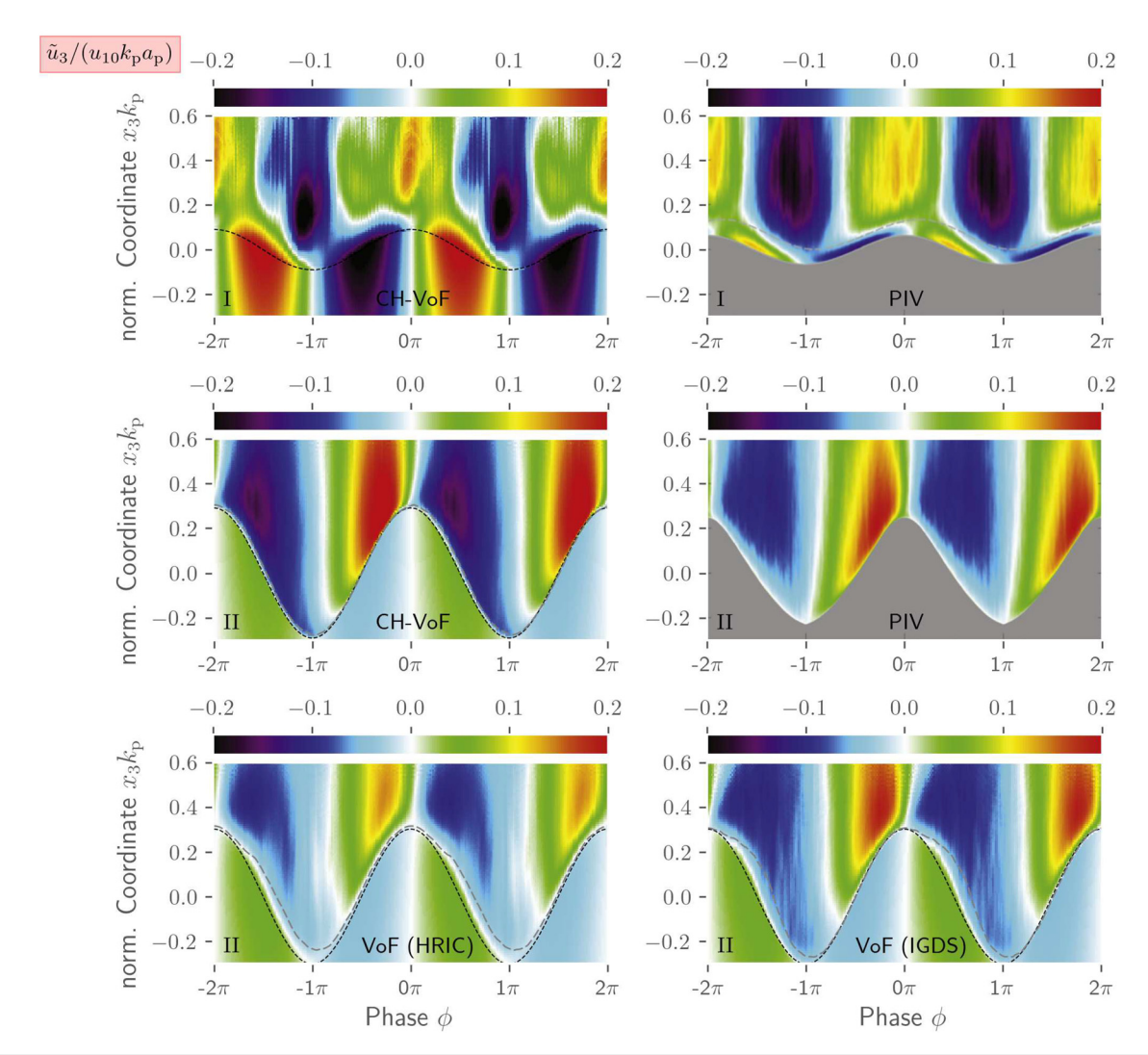


FIG. 7. Comparison of (laterally averaged) normalized horizontal wave-coherent velocity fields $\tilde{u}_3/(u_{10}k_pa_p)$ as a function of vertical coordinate x_3k_p and the phase position ϕ . Top and center row: The results obtained from the present simulations (CH–VoF, left) and the experiments of Buckley and Veron⁴³ (PIV; right) for a low (scenario I; top) and a high wind speed wave (scenario II; center). Bottom row: Supplementary results obtained from classical VoF simulations using different convective approximations: HRIC (left) and IGDS (right). Dashed gray line indicates the height of the critical layer. Coloring is restricted to the measurement data, which is partly only available as images. For illustration, an alternative coloring is used in Appendix B. Reproduced with permission from Buckley and Veron, Eur. J. Mech.-B/Fluids **73**, 132–143 (2019). Copyright 2019 Elsevier

upstream-directed phase lag of approximately $\pi/2$ in the experiments for the low wind speed wave (I, top), which is not fully recovered by the simulations. The most distinct feature of the low (high, II) wind speed scenario is the phase jump of $\pi/2$ (π) observed for \tilde{u}_3 when crossing the free surface. Since the height of the critical layer is not negligible for the low wind speed case (I, top), we observe an asymmetry of the air-phase velocity above and below the critical layer height, which was also reported in the experiments and expected from Miles critical layer theory. In accordance with experiments, the computed airflow at the interface is directed down (up) for the upstream (downstream) face for the low wind speed wave (I), and an opposite trend is observed for the high wind speed wave (II).

An interesting comparison involves the lower two rows of Figs. 6 and 7, which display the wave coherent horizontal and vertical velocities predicted by two classical VoF methods (bottom row) and the present CH–VoF approach (center row) for the high wind speed wave (II). The comparison reveals predictive improvements of the CH–VoF methods primarily related to the leeward behavior of the critical layer. Different from the CH–VoF data, both VoF results depict a sudden increase in the leeward critical layer due to the injection of high-density fluid parts from the interface layer into the airflow. A deeper analysis of the predictive disparities between the VoF and the CH–VoF reveals a sharp but much more rippled/rugged interface of the former in the vicinity of the crest. This observation is independent

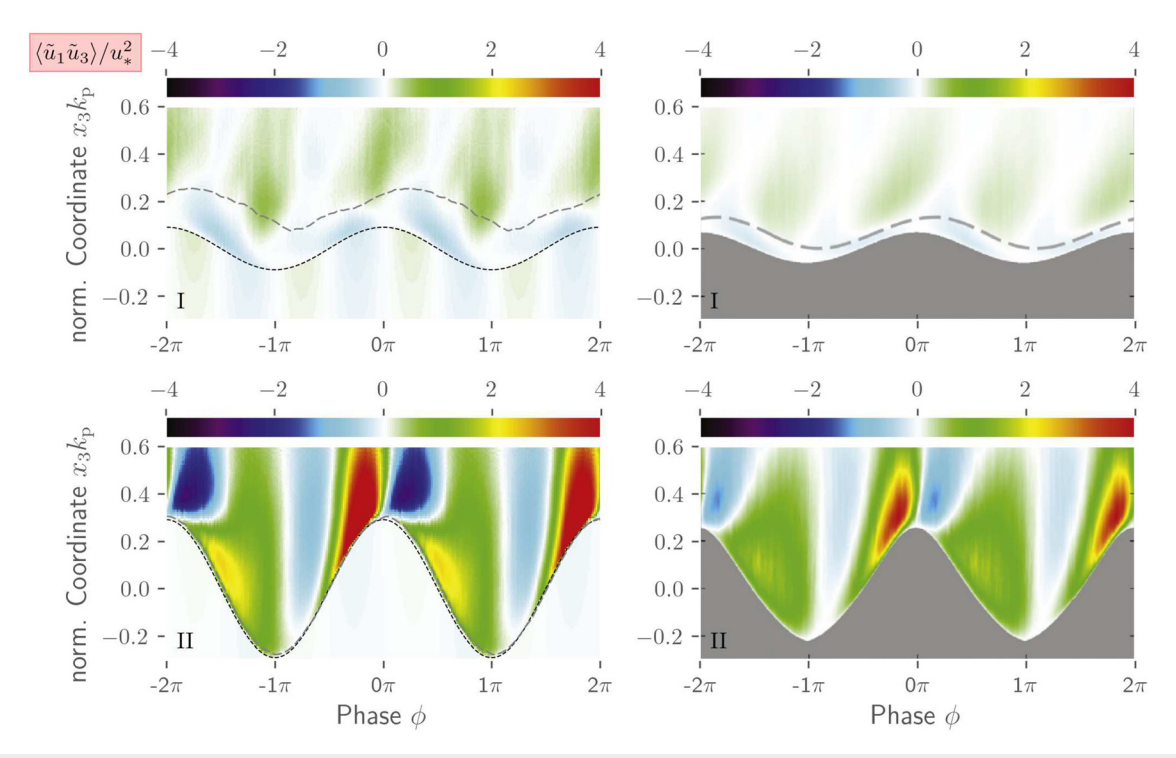


FIG. 8. Comparison of (laterally averaged) normalized wave-coherent shear stresses $\langle \tilde{u}_1 \tilde{u}_3 \rangle / u_*^2$ as a function of the vertical coordinate $x_3 k_p$ and the phase position ϕ obtained from the present simulations (left) and experiments of Buckley and Veron⁴³ (right) for a low (scenario I; top) and a high wind speed wave (scenario II; bottom). Dashed gray line indicates the height of the critical layer. Coloring is restricted to the measurement data, which is partly only available as images. For illustration, an alternative coloring is used in Appendix B. Reproduced with permission from Buckley and Veron, Eur. J. Mech.-B/Fluids **73**, 132–143 (2019). Copyright 2019 Elsevier B.V.

of the convective approximation used for the VoF simulations (HRIC, IGDS). These small-scale ripples vary in space and time, and the flow field (occasionally) reveals strong local accelerations that are inclined against the wavy interface and promote separation. In a continuous limit, we expect similar results from a VoF and a CH-VoF framework. Hence, the results of Fig. 6 indicate the technical benefits of the CH-VoF approach, e.g., a minor grid dependency and a less rugged prediction of the free surface in under-resolved flows. Mind that, in contrast to the CH–VoF, the compressive face-property reconstruction schemes of many VoF methods are prone to interferences by the local Courant number and the inclination of the interface against the cellface normal. The maximum Courant number, however, never increased above Co = 0.22 in the present study. Moreover, the CH-VoF approach has resharpening capabilities, as indicated in Kühl, Hinze, and Rung,²⁵ which can be a crucial asset of the modeling approach. Note that the EoS of the VoF simulations is in the linear form, cf. Eq. (7).

To assess the wave-induced momentum fluxes, we display the mean wave-coherent shear stresses $\langle \tilde{u}_1 \tilde{u}_3 \rangle$ in Fig. 8. Experimental and numerical results again reveal a fair predictive agreement. Simulated shear stress magnitudes are larger than the corresponding experimental values above the critical layer. The comparison between the two scenarios reveals a more symmetric shear stress distribution upstream and downstream of the crest near the free surface for the low wind speed case (I) displayed in the top sub-figures. This turns into more obvious disparities between locations featuring

similar ϕ in the critical layer and above. Following the reduction of the critical layer height, a pronounced asymmetry of the wave-coherent shear stress around the crest is observed on the air side for the high wind speed scenario (II, bottom), which is also confirmed by experimental observations. This also results in significantly different forces on the upstream and downstream faces, which drive the wave train.

C. Mean horizontal velocity and pressure

Figure 9 compares the predicted (left) and measured (right) mean horizontal velocity. While the far-field measurements are reproduced well, mixing-inducing (turbulent) dynamics is apparently missing in the predictions close to the free surface. The issue is observed in both scenarios and results in a generally thicker air-phase boundary layer above the wavy interface. However, the simulations capture the relative difference between the two scenarios, and the phase-related pattern is predicted with reasonable accuracy.

The observation is confirmed by the above discussion on the critical layer and a comparison of the mean velocity profiles, presented on the left side of Fig. 10. Here, small disparities between predictions and measurements are also pronounced close to the interface for the mean velocity and the Reynolds stresses. The reason for the deficit is attributed to inconsistent and too-low levels of approach flow turbulence, which is verified by comparing the turbulent stresses in Sec. VE and would suggest employing scale-resolving inlet conditions. Nevertheless, the vertical profiles from experiment and simulation

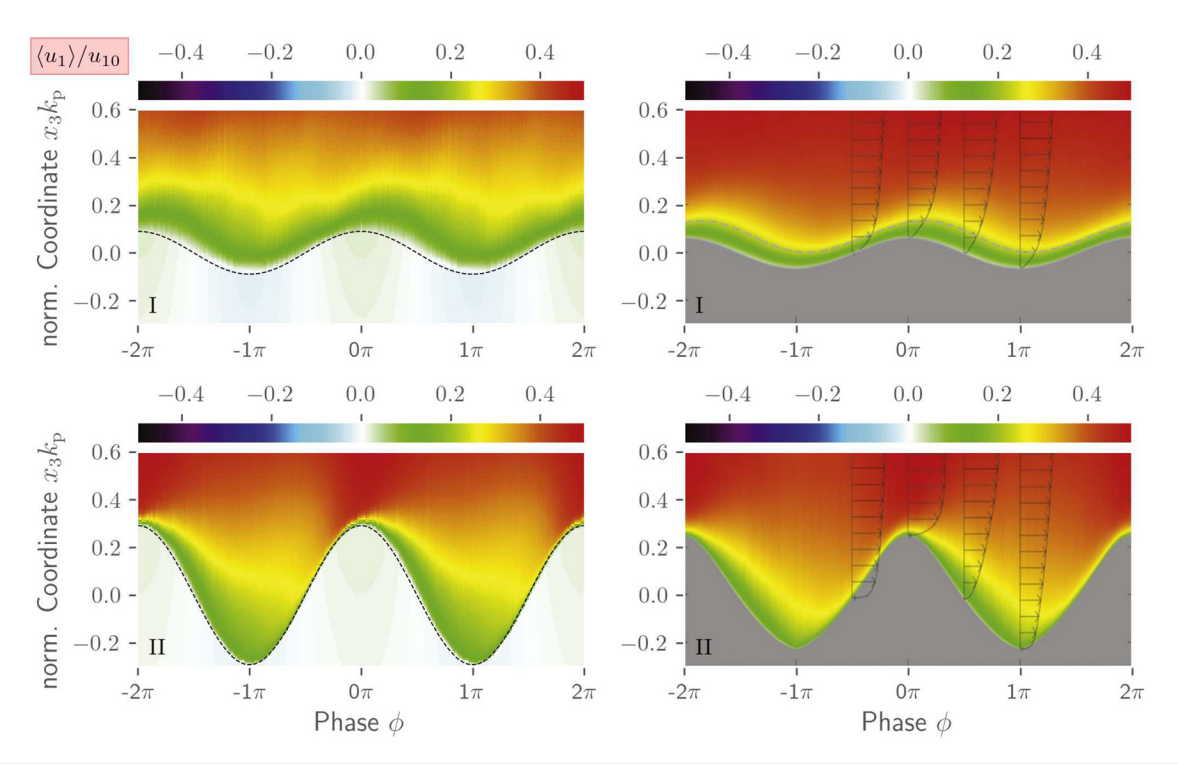


FIG. 9. Comparison of (laterally averaged) normalized mean horizontal velocity $\langle u_1 \rangle / u_{10}$ as a function of the vertical coordinate x_3k_p and the phase position ϕ obtained from the present simulations (left) and the experiments of Buckley and Veron⁴³ (right) for a low (scenario I; top) and a high wind speed wave (scenario II; bottom). Reproduced with permission from Buckley and Veron, Eur. J. Mech.-B/Fluids **73**, 132–143 (2019). Copyright 2019 Elsevier B.V.

agree very well, so that different trends of the respective wind-wave conditions can be clearly detected.

An evaluation of the averaged pressure supplements the wavecoherent shear stress for the wave drag analysis. The pressure contours and surface pressures displayed in Fig. 11 confirm the fair predictive agreement observed before. For the low wind speed case shown in the top sub-figures, the upstream face of the wave is exposed to positive pressures, and the downstream face experiences negative pressure. The pressure distributions of simulation and experiment are of remarkable similarity, while the simulated magnitudes are slightly more elevated.

When attention is directed to the high wind speed cases (II, III) depicted by the bottom sub-figures, only a smaller regime in the vicinity of the crest is exposed to negative pressures, and the negative pressure regime is tilted slightly downstream in the experiments and simulations. Again, measured and predicted surface pressures are in remarkable agreement. Due to the different wave scenarios (II, III), we omit discussing further details of the pressure contours herein.

D. Form drag and surface stress

The form drag per unit area $\bar{\tau}_D$ is approximated by a well known relation, derived from a horizontal momentum budget, ⁴⁹ viz.,

$$\bar{\tau}_{\mathrm{D}} = \overline{p \frac{\partial \hat{\eta}}{\partial x_{1}}},\tag{39}$$

with $\hat{\eta}$ representing smoothed surface elevation, cf. Sec. III A. In line with Funke *et al.*, ⁴⁹ the overbar denotes the phase averaging process

according to Eq. (37). The computed non-dimensional form drag $\bar{\tau}_D/(\rho u_*^2)$ reads 0.18 (0.69) for the first (second) scenario and approximately agrees with the literature published data for similar wave ages and slopes discussed in Wu, Popinet, and Deike¹⁶ and Funke *et al.*,⁴⁹ cf. Table IV.

In line with Buckley, Veron, and Yousefi,⁵¹ the average total surface stress $\bar{\tau}_s$ is expected to be approximately equal to the surface friction $\rho_{\rm air}u_*^2$ used for wind forcing, i.e.,

$$\rho_{\rm air} u_*^2 \approx \bar{\tau}_{\rm s} = \bar{\tau}_{\nu}^* + \bar{\tau}_{\rm D},\tag{40}$$

where $\bar{\tau}_{\nu}^{*}$ and $\bar{\tau}_{D}$ denote the viscous stress at the surface and the form drag as described in Eq. (39). However, due to the diffusive interface approach and the related lack of an explicit interface, an accurate calculation of viscous surface stresses is challenging in the simulations. Therefore, the latter is reconstructed from the difference of the form drag and the total stress, which follows from a horizontal momentum balance of the air phase, viz.,

$$\bar{\tau}_s \Leftarrow \frac{\mathrm{d}\hat{I}_1}{\mathrm{d}t} = \sum_{i=1}^n \hat{f}_{1,j}.\tag{41}$$

Here, \hat{I}_1 and $\hat{f}_{1,j}$ refer to the horizontal momentum and the horizontal forces acting at the air phase, which includes both pressure and viscous forces. The momentum balance is evaluated for each time step to estimate the mean total surface drag within the study area of the domain. In contrast to this, Funke $et\ al.^{49}$ did measure $\bar{\tau}_{\nu}^*$ and reconstruct $\bar{\tau}_D$ from the experimental data.

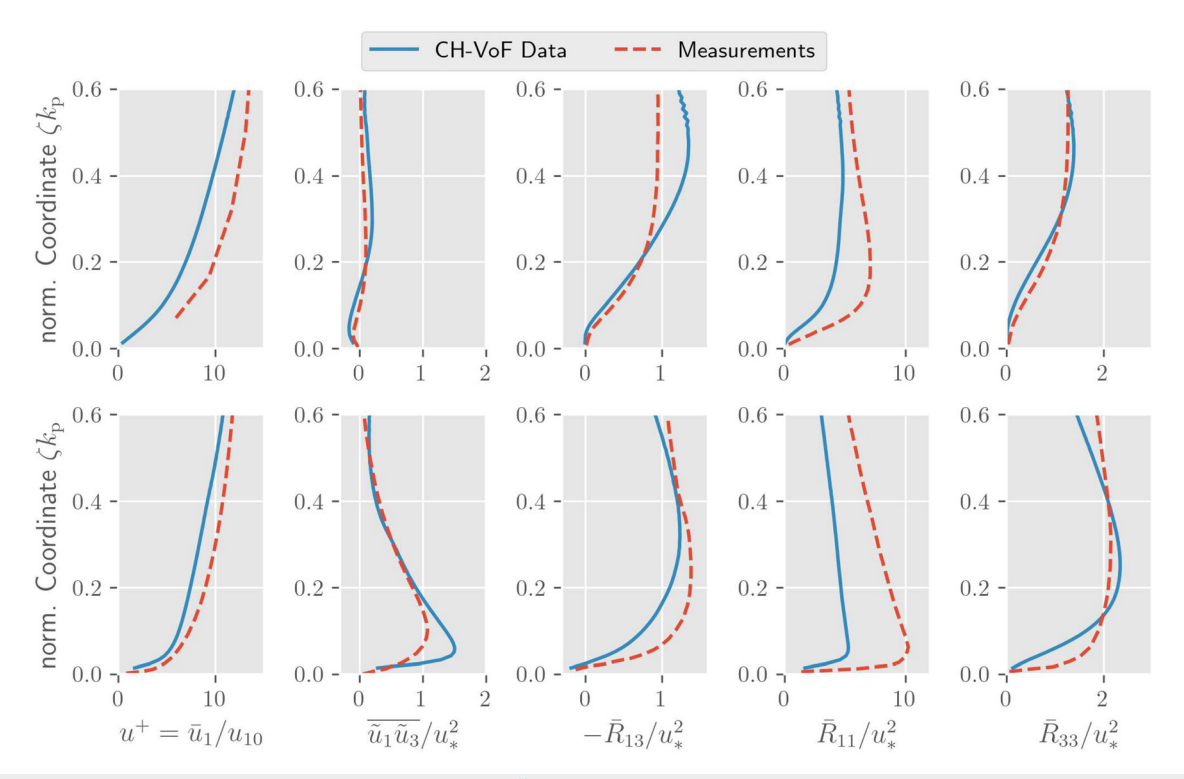


FIG. 10. Comparison of predicted (blue) and measured (Buckley and Veron;⁴³ red) vertical profiles for total mean (for all phases) quantities for a low (scenario I; top) and a high wind speed wave (scenario II; bottom); from the left to the right: Non-dimensional mean velocity $u^+ = \bar{u}_1/u_*$, non-dimensional wave-coherent shear stress $\bar{u}_1,\bar{u}_3/u_*^2$ as well as normalized Reynolds shear and normal stresses $-\bar{R}_{13}/u_*^2$, \bar{R}_{11}/u_*^2 and \bar{R}_{33}/u_*^2 . Reynolds stresses are defined by Eq. (42). Reproduced with permission from Buckley and Veron, Eur. J. Mech.-B/Fluids **73**, 132–143 (2019). Copyright 2019 Elsevier B.V.

Resulting total and viscous stresses are also reported in Table IV. Generally, the predictions of the total stresses and their distribution to the two individual contributions are in fair agreement with experimental observations. In particular, the trend toward increasing form drag at higher wave slopes is clearly discernible in both the simulation and the experiment. The less pronounced bias of the computed total drag toward the viscous stress in the first scenario (I) could be explained by the slightly higher wave slope in the simulations, cf. Table I. An advantage of the simulation is the direct access to pressure which does not need to be reconstructed elaborately during post-processing.

E. Reynolds stresses

Unlike all previous investigations, e.g., Hara and Sullivan, ⁴⁷ Sullivan *et al.*, ³ Husain *et al.*, ⁷ or Wu, Popinet, and Deike, ¹⁶ the present study employs a hybrid RANS-LES (DES) turbulence modeling approach. The advantage of the method is the lower resolution requirement to compute high Reynolds number flows, all the more so when future applications of field data measurements turn out to be more complex than an experimental wind–wave flume. As indicated by Fig. 12, the turbulence model is in the LES mode in almost all areas of the computational domain, and the RANS mode is only activated near the interface and below where the interface is diffusive. Therefore, on average, the RANS layer only spans about three cells in the vertical direction for both scenarios.

This section compares measured and predicted Reynolds stresses R_{ik} . The simulated Reynolds stresses consist of two components, the modeled stresses R_{ik}^{mod} and the resolved stresses R_{ik}^{res} , viz.,

$$R_{ik} = R_{ik}^{\text{mod}} + R_{ik}^{\text{res}}$$

$$= -2\langle \nu^{t} S_{ik} \rangle + \frac{2}{3} \langle \hat{k} \rangle \delta_{ik} + \langle u'_{i} u'_{k} \rangle^{\text{res}}.$$
(42)

Contour plots of the normalized shear stresses $-R_{13}/u_*^2$ are depicted in Fig. 13. Both cases presented herein exhibit negative (upward-directed) stresses along the upwind face of the waves. Along the downwind face of the waves, neutral (I) or positive (downward-directed, II) stresses occur, as captured by both experiments and computations.

For the first scenario, peak values of the numerical results exceed peak values reported from the experiments, but the computed stress levels show a fairly similar distribution to experimental values in the bulk of the flow. In contrast, the stress levels near the interface along the leeward and windward sides are slightly below the experimental stresses, confirming the observation from Fig. 10. With attention directed to the high wind speed scenario at the bottom of Fig. 13, this disparity between simulations and experiments at the interface becomes more pronounced on the windward side of the waves. However, the general features of the two shear-stress fields are (again) very similar. For the high wind speed waves, on average, an intensification of the turbulent stresses on the leeward side of the waves is

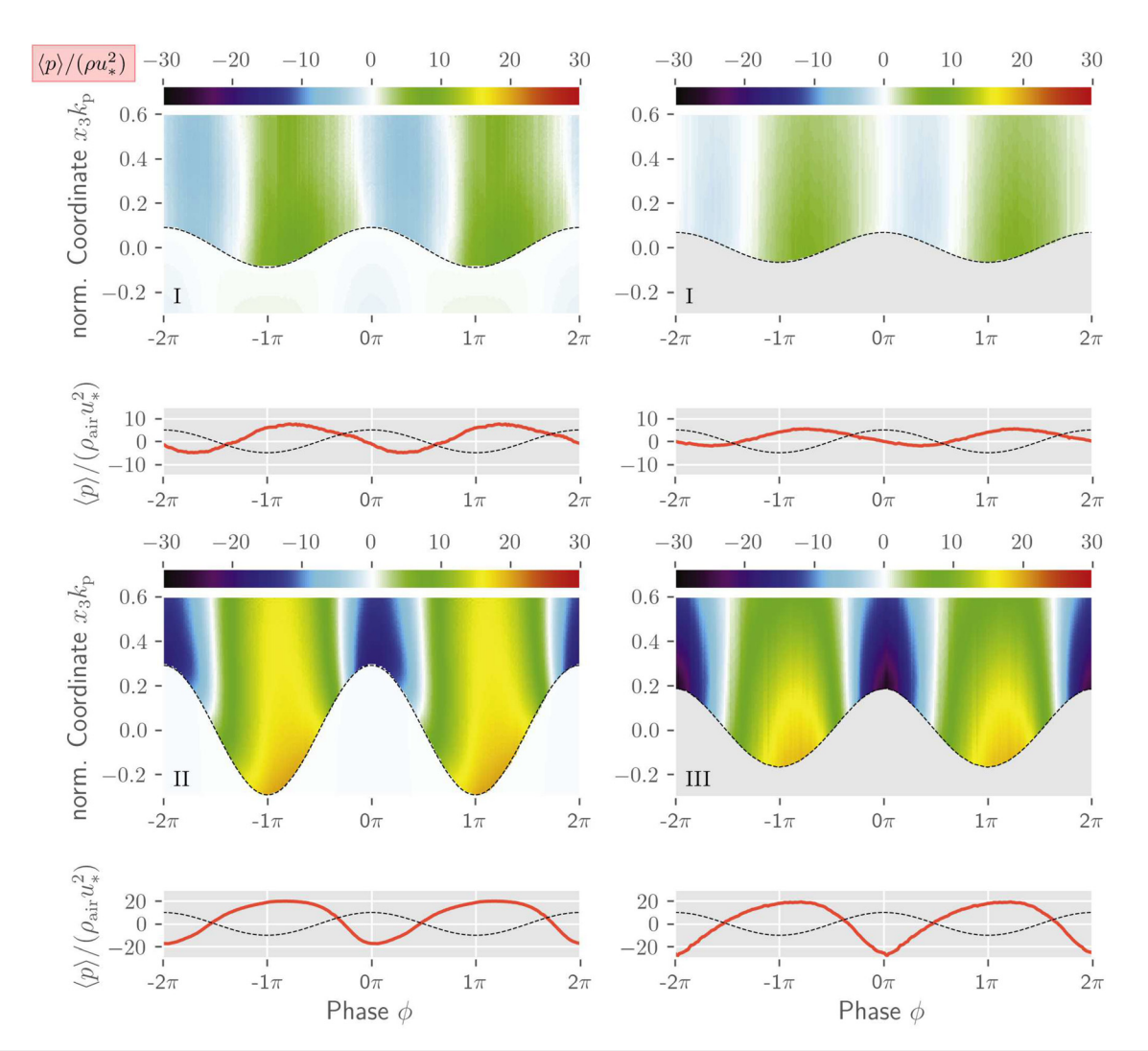


FIG. 11. Comparison of (laterally averaged) normalized averaged pressure fields $\langle p \rangle / (\rho u_*^2)$ as a function of the vertical coordinate x_3k_p and the phase position ϕ obtained from the present simulations (left) and experiments of Funke *et al.*⁴⁹ (right) for a low (scenario I; top) and a high wind speed wave (scenarios II and III; bottom). Normalized pressure distribution at the air–sea interface are shown below the contour plots. Reproduced with permission from Buckley and Veron, J. Phys. Oceanogr. **51**, 3449–3460 (2021). Copyright 2021 American Meteorological Society.

observed by the experiments and (to a slightly smaller extent) the simulations.

The missing description of the approach flow turbulence becomes more apparent when comparing the horizontal and vertical **TABLE IV.** Comparison of simulated and experimentally reported normalized mean surface stresses, cf. Funke *et al.*, 49 by means of total surface stress $\bar{\tau}_s$, form drag $\bar{\tau}_D$ and viscous stress $\bar{\tau}_\nu^*$.

	$a_{\rm p}k_{\rm p}$		$\overline{ au}_{\mathrm{s}}/(ho_{\mathrm{air}}u_{*}^{2})$		$\bar{ au}_{\mathrm{D}}/(\mu$	$o_{\rm air}u_*^2)$	$\overline{ au}_{ u}^*/(ho_{ m air}u_*^2)$		
Scenario	Sim.	Exp.	Sim.	Exp.	Sim.	Exp.	Sim.	Exp.	
I	0.09	0.07	0.90	1.01	0.18	0.15	0.72	0.86	
III		0.19		1.05		0.65		0.40	
II	0.28	0.27	1.00	• • • •	0.69	• • • •	0.31	• • • •	

normal stresses R_{11}/u_*^2 and R_{33}/u_*^2 in Figs. 14 and 15. The predicted R_{11}/u_*^2 fields agree qualitatively for the low wind speed wave (I) with experiments. However, above the wave's crest on the windward side, the stress levels are underestimated. This becomes more significant for the high wind speed case (II), where the simulation results show significantly smaller areas of high stress.

The vertical normal stresses R_{33}/u_{\ast}^2 shown in Fig. 15 reveal a better agreement between the experimental and numerical data, though the stress level is generally much smaller than for the horizontal normal stresses. Again, differences are pronounced near the free surface, especially for the second scenario on the windward side of the waves. Mind that only minimal levels of turbulent dynamics are observed in the water phase during the simulations, which might also be a reason for the differences between the measurements and the predictions. A more detailed description of the incoming flow turbulence seems

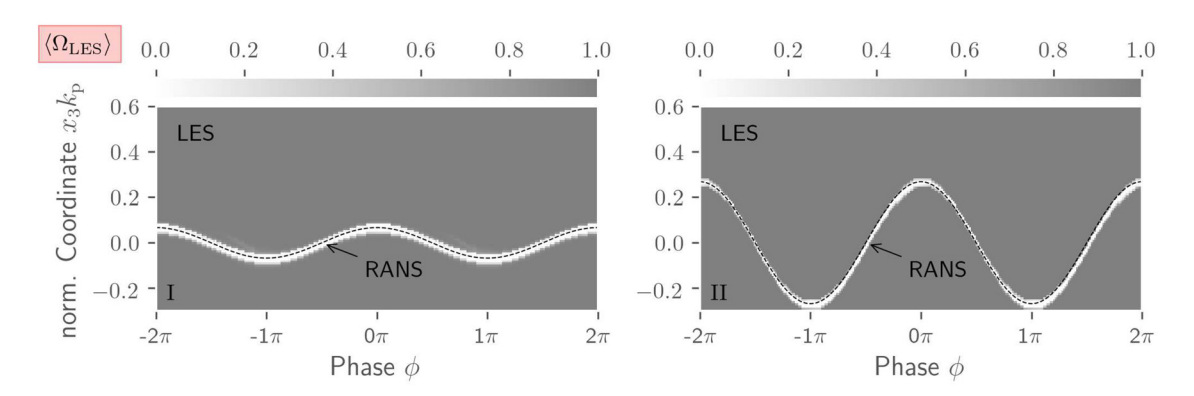


FIG. 12. Comparison of LES indicator function $\langle \Omega_{\text{LES}} \rangle$ as defined in Eq. (26) [i.e., $\langle \Omega_{\text{LES}} \rangle = 1 \rightarrow \text{LES}$; $\langle \Omega_{\text{LES}} \rangle = 0 \rightarrow \text{RANS}$] as a function of the vertical coordinate x_3k_p and the phase position ϕ for a low (scenario I; left) and a high wind speed wave (scenario II; right).

necessary to better reproduce realistic near-surface dynamics of the experiments.

VI. CONCLUSION AND OUTLOOK

This paper scrutinizes the ability of a diffusive interface (CH–VoF) two-phase flow model to capture air–sea interface phenomena. The model comprises a pressure-based, second-order accurate FV procedure that involves a hybrid filtering/averaging (DES) approach to model flow turbulence, and is capable of simultaneously

simulating atmosphere and ocean coupling through the surface wave field at realistic Reynolds numbers with surface tension.

Attention is devoted to two different wind-wave conditions, referring to fairly young wave ages ($C_{\rm p}/u_*<10$) with different wave slopes and wind speeds, where extensive experimental results were reported in a series of papers by Buckley and Veron^{41–43} and Funke *et al.*⁴⁹ Generally, the predictions are in good agreement with measurements, though the height of the critical layer is over-predicted in both cases and the shape reveals small inaccuracies above the trough for the

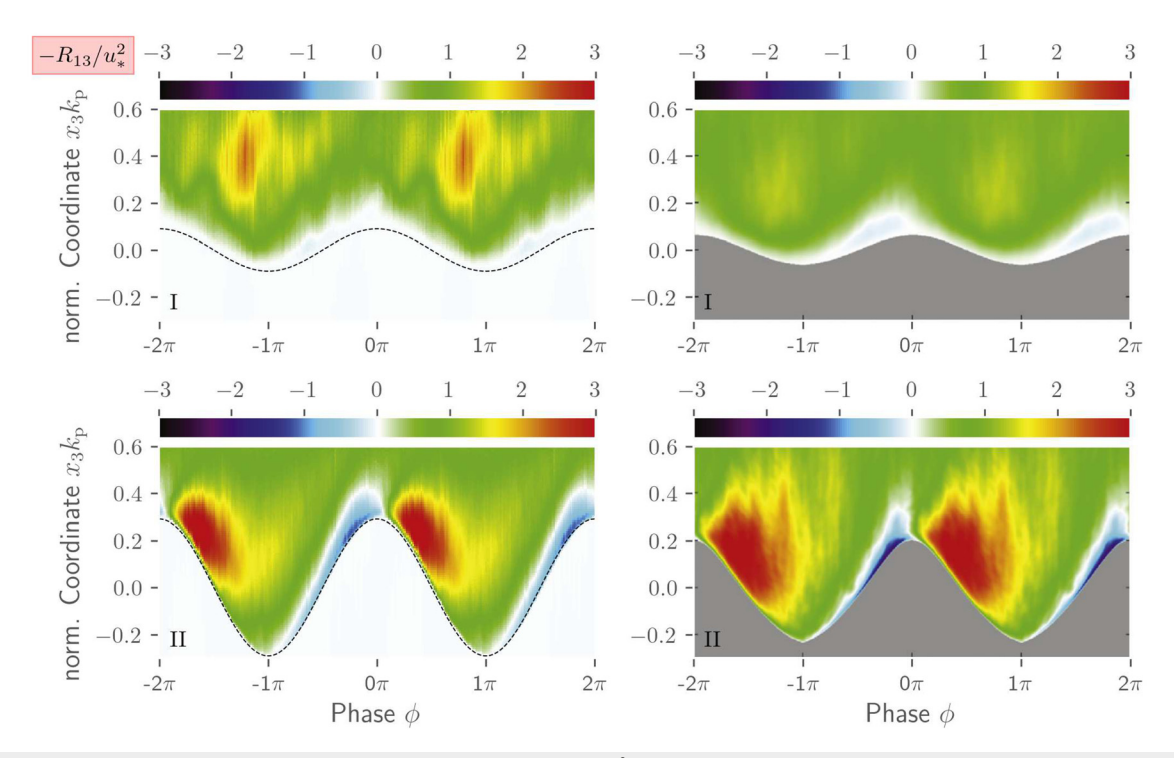


FIG. 13. Comparison of (laterally averaged) normalized Reynolds shear stresses $-R_{13}/u_*^2$ as a function of the vertical coordinate x_3k_p and the phase position ϕ obtained from the present simulations (left) and the experiments (Buckley and Veron; ⁴³ right) for a low (scenario I; top) and a high wind speed wave (scenario II; bottom). Reproduced with permission from Buckley and Veron, Eur. J. Mech.-B/Fluids **73**, 132–143 (2019). Copyright 2019 Elsevier B.V.

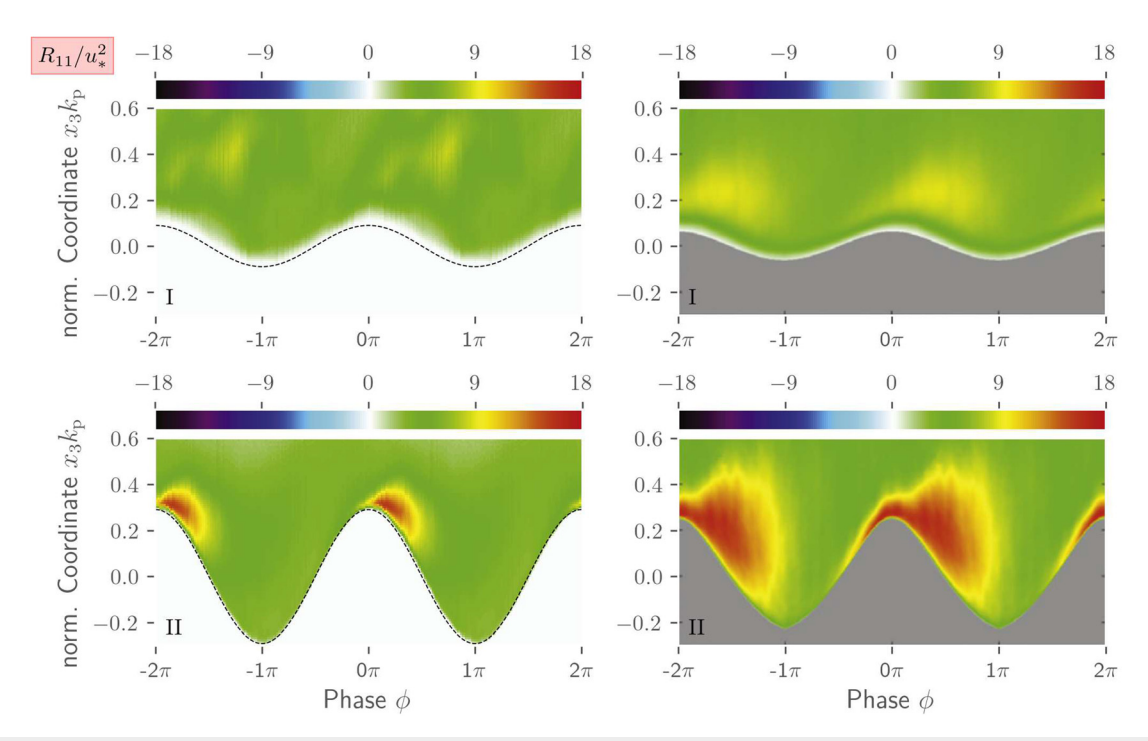


FIG. 14. Comparison of (laterally averaged) normalized Reynolds normal stresses R_{11}/u_*^2 as a function of the vertical coordinate x_3k_p and the phase position ϕ obtained from the present simulations (left) and the experiments (Buckley and Veron; ⁴³ right) for a low (scenario I; top) and a high wind speed wave (scenario II; bottom). Reproduced with permission from Buckley and Veron, Eur. J. Mech.-B/Fluids **73**, 132–143 (2019). Copyright 2019 Elsevier B.V.

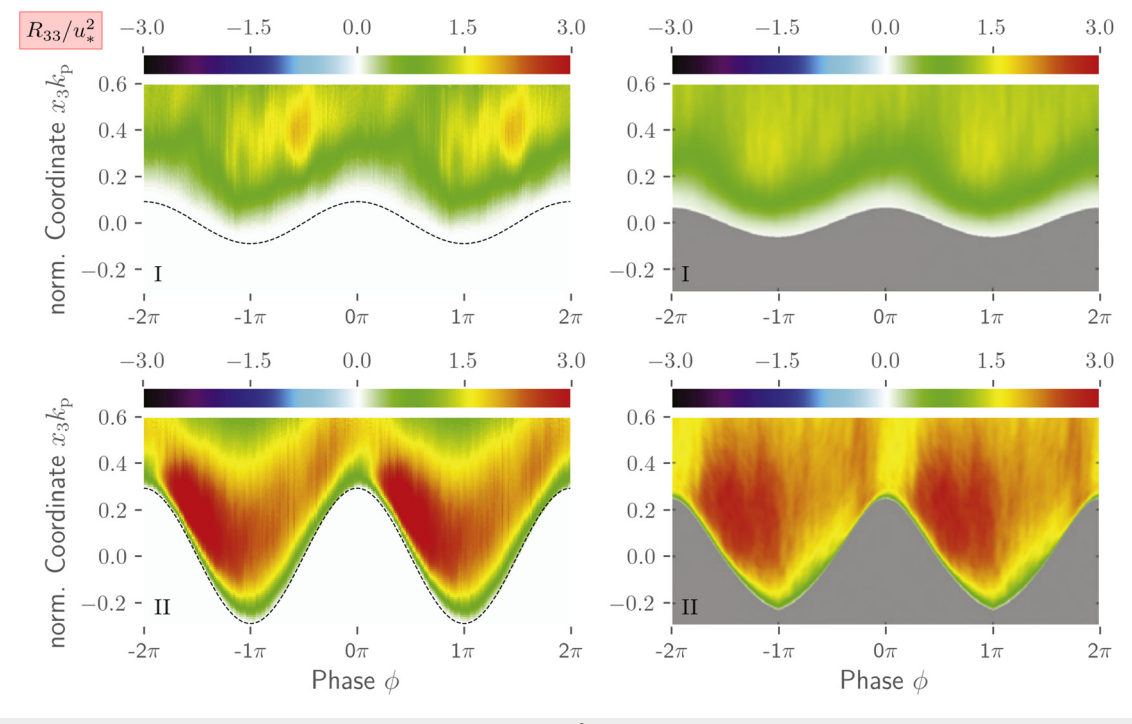


FIG. 15. Comparison of (laterally averaged) normalized Reynolds normal stresses R_{33}/u_*^2 as a function of the vertical coordinate x_3k_p and the phase position ϕ obtained from the present simulations (left) and the experiments (Buckley and Veron;⁴³ right) for a low (scenario I; top) and a high wind speed wave (scenario II; bottom). Reproduced with permission from Buckley and Veron, Eur. J. Mech.-B/Fluids **73**, 132–143 (2019). Copyright 2019 Elsevier B.V.

low wind speed wave. The high wind speed (steep) case features a very thin critical layer and a large sheltering effect, where turbulent stresses are significantly augmented compared to the surrounding flow. The prediction of these phenomena is not as pronounced as the experimental data indicate. Nonetheless, the computations recover the (intermittent) occurrence of airflow separation downstream of the high wind speed wave crest, in line with a more disordered vorticity field, and also display a related increase in turbulence intensity downstream of the crests produced by detached shear layers. For the less steep, low wind speed case, the height of the predicted critical layer substantially increases, as also reported by the experiments. Similar to the experiments, the wave coherent air velocities below the critical layer start to display an asymmetry with respect to the airflow above the critical layer. As the wave gets older, we can also see a strong coupling of the near-surface airflow with the water motions inside the critical laver.

The study points out the dynamical role of the airflow motions around the critical layer for relatively young waves, in line with the work of Carpenter, Buckley, and Veron. This is in spite of the non-negligible turbulence observed in the airflow within the present simulations, including typical turbulent boundary layer phenomena (ejections and sweeps, detaching spanwise vorticity structures). Comparing the two scenarios, numerical results predict a reduction of turbulent stress magnitudes with increasing wave age (decreasing wave slope), which is compensated in parts by wave coherent stresses that transit through the free surface into the thicker critical layer. The pressure contours reveal a significant phase shift and indicate the large influence of the wave slope on the pressure distribution at the surface, respectively, the form drag. Simulated viscous stress and form drag agree very well with the experimental data.

The present numerical approach presents the potential for a future detailed study of the competing contributions of turbulent processes vs mean wave-coherent motions to wave growth. ⁵³ We have identified the specification of inflow turbulence as an important parameter that can influence the distributions of Reynolds stresses and critical layer heights for younger wave ages, although the basic phase averaged distributions of all quantities are well represented by the simulations.

The development of this model, with its capability to fully capture coupled atmosphere-ocean dynamics on turbulence-resolving scales, opens up many possibilities for the study of upper ocean and lower atmosphere turbulent processes that have been notoriously difficult to access. Such processes include energy and momentum fluxes in wave breaking regimes, surface wave phase-resolved Langmuir turbulence, and wind-wave generation mechanisms. Such studies will form the subject of future investigations.

ACKNOWLEDGMENTS

This paper is a contribution to the project T4 ("Surface Wave-Driven Energy Fluxes at the Air-Sea Interface") of the Collaborative Research Centre TRR 181 "Energy Transfers in Atmosphere and Ocean" funded by the Deutsche Forschungsgemeinschaft (DFG, German Research Foundation)—Grant No. 274762653.

Publishing fees supported by Funding Programme Open Access Publishing of Hamburg University of Technology (TUHH).

The authors gratefully acknowledge the computing time granted by the Resource Allocation Board and provided on the supercomputer Lise and Emmy at NHR at ZIB and NHR at Göttingen as part of the NHR infrastructure. The calculations for this research were conducted with computing resources under the Project No. hhi00037 ("Energy Fluxes at the Air–Sea Interface").

AUTHOR DECLARATIONS

Conflict of Interest

The authors have no conflicts to disclose.

Author Contributions

Malte Ole Loft: Conceptualization (equal); Formal analysis (lead); Investigation (equal); Methodology (equal); Software (lead); Validation (lead); Visualization (lead); Writing – original draft (equal); Writing – review & editing (equal). Niklas Kühl: Conceptualization (equal); Methodology (equal); Software (equal); Writing – original draft (equal); Writing – review & editing (equal). Marc P. Buckley: Data curation (equal); Methodology (equal); Writing – review & editing (equal). Jeffrey Richard Carpenter: Data curation (equal); Methodology (equal); Writing – review & editing (equal). Michael Hinze: Methodology (equal); Writing – review & editing (equal). Fabrice Veron: Data curation (equal); Writing – review & editing (equal). Thomas Rung: Conceptualization (lead); Investigation (equal); Methodology (equal); Project administration (lead); Resources (equal); Software (equal); Supervision (lead); Writing – original draft (equal); Writing – review & editing (equal).

DATA AVAILABILITY

The data that support the findings of this study are available from the corresponding author upon reasonable request.

NOMENCLATURE

Abbreviations

CFD computational fluid dynamics

CH Cahn-Hilliard

DES detached eddy simulation

DNS direct numerical simulation

EoS equation of state

FV finite-volume

HPC high performance computing

HRIC high resolution interface-capturing

IDDES improved delayed detached eddy simulation

IGDS inter gamma differencing scheme

ITTL implicit three time level

LES large eddy simulation

PDE partial differential equation

PIV particle image velocimetry

PSD power spectral density

RANS Reynolds averaged Navier-Stokes

RHS right-hand side

SIMD single instruction multiple data

SST shear stress transport

turbulent kinetic energy TKE VoF volume-of-fluid

Lower-case latin

wave amplitude a, a_p

turbulence model constant a_1

h double-well potential

concentration c, c_i

smoothed concentration

turbulence model constant $c_{
m DES}$

bulk-correction coefficient c_{in}

turbulence model constants $c_{\rm l}, c_{\rm t}$ turbulence model constants $c_{\rm w}, c_{\rm dt}$

turbulence model constant c_{μ}

surface distance d

auxiliary variable d

Euler's number

wave frequency

horizontal forces

aggregation function

forcing

acceleration of gravity

complex number

 k, k_p wave number

turbulent kinetic energy

non-dimensional function m, m^{j}

face normal vector

pressure p, p^{J}

time

 u_i velocity

friction velocity

 u^+ dimensionless velocity

characteristic "10 m" velocity u_{10}

coordinate

 y^+ dimensionless wall distance

 z_0 roughness length

Upper-case latin

 A^{j} main diagonal coefficient

C,C_p phase velocity

Courant number Co

 C_1 , C_2 Cahn-Hilliard constants

 F_i , \hat{F}_i parameters, blending functions

horizontal momentum

 L_i length scale

Mmobility parameter

 $N_{\mathrm{avg}} P^{\mathrm{k}}$ data-processing wave periods

production of TKE

 R, R^j residuum

Reynolds stresses R_{ik}

 Re_{λ} Reynolds number

 S, S_i surface

strain rate tensor

 S_{ik} S^{j} source term, RHS

Ttemperature

data averaging time control volume W_{ik} rotation rate tensor

Lower-case greek

 α , β turbulence model constants

 α_s, β_s empirical parameters

 $\alpha_{\hat{d}}, \beta_{\hat{d}}, \beta_{\hat{d}}^*$ empirical parameters

turbulence model constant

interface thickness

transition parameter

Kronecker delta

vertical coordinate

smoothed surface elevation $\hat{\eta}$

analytic signal $\eta_{\rm a}$

Von-Karman constant к

curvature κ_{σ}

λ, λρ wave length

dynamic viscosity μ , μ_i^i

 $\mu^{\acute{\Delta}}$ dynamic viscosity difference

kinematic viscosity ν

interface viscosity

density ρ, ρ_i^i

mass transfer rates $\dot{\rho}_i$

 $ho^{\acute{\Delta}}$ density difference

 σ surface tension

turbulence model constants $\sigma_{\omega}, \, \sigma_{\mathrm{k}}$

form drag $\bar{\tau}_{\mathrm{D}}$

total surface stress

viscous stress

generic variable or coefficient

wave phase

ψ chemical potential

wave angular frequency ω , ω_{p}

specific turbulent kinetic energy dissipation rate

vorticity ω_2

Upper-case greek

diffusivity

 Δ, Δ_i edge length or delta

Θ heaviside step function

Λ far-field

indicator function Ω_{LES}

Sub- and superscripts

fluid a or analytic

air phase air

averaged avg

fluid bb

BR Brackbill

critical crit

СН Cahn-Hilliard

D drag

eff effective

- f face index
- *i*, *j*, *k* indices, placeholder
 - l laminar
- mod modeled or modified
 - p peak frequency
 - P cell center index
 - res resolved
 - s surface

- sea sea/water phase ST surface tension
- t turbulent, time
- 1, 2, 3 horizontal, lateral and vertical direction

Operators and specials

 $\mathscr{F}(\cdot)$ Fourier transformation

TABLE V. Brief summary of all modeling constants (IDDES).

	c_{μ}	К	eta^*	a_1	$c_{ m DES}$	α	β	$\sigma_{ m k}$	σ_{ω}	c_{w}	$c_{ m dt}$	c_{l}	c_{t}
φ_1 φ_2	0.09	0.41	0.09	0.31	0.78 0.61	5/9 0.44	0.075 0.0828		0.5 0.856	0.15	20	5.0	1.87

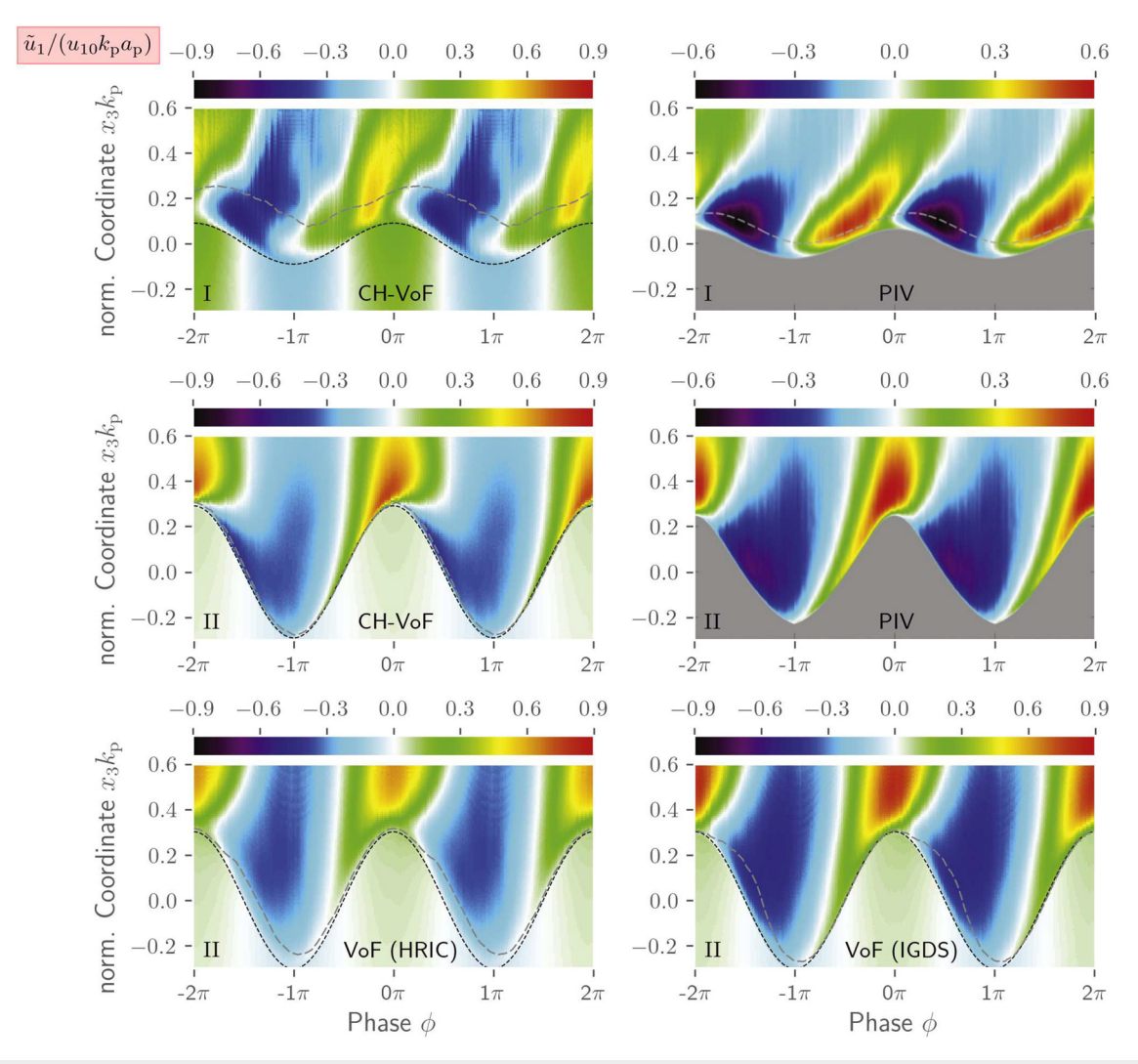


FIG. 16. Similar plots as Fig. 6 with adapted coloring. Reproduced with permission from Buckley and Veron, Eur. J. Mech.-B/Fluids 73, 132–143 (2019). Copyright 2019 Elsevier B.V.

- $\mathcal{H}(\cdot)$ Hilbert transformation
- $\Im \mathfrak{m}(\cdot)$ imaginary part
- $\mathscr{L}(\cdot)$ filtering operator
- $max(\cdot)$ maximum value
- $min(\cdot)$ minimum value
 - $\langle (\cdot) \rangle$ mean
 - $\overline{(\cdot)}$ phase averaged mean
 - (.) wave coherent
 - $(\cdot)'$ fluctuation

APPENDIX A: BLENDING FUNCTIONS AND PARAMETERS OF THE IDDES MODEL

The following equations represent the blending functions of the IDDES model used in this study. Equations and parameters agree with a model variant of Gritskevich *et al.*³⁷

$$F_{1} = \tanh\left(\left(\min\left[\max\left[\frac{\sqrt{\hat{k}}}{\beta^{*}\hat{\omega}d}, \frac{500\nu}{d^{2}\hat{\omega}}\right], \frac{2\rho\hat{\omega}}{d^{2}\frac{\partial\hat{k}}{\partial x_{k}}\frac{\partial\hat{\omega}}{\partial x_{k}}}\right]\right)^{4}\right), \quad (A1)$$

$$F_2 = \tanh\left(\max\left[\frac{2\sqrt{\hat{k}}d}{\hat{\omega}\beta^*}, \frac{500\mu}{\rho}\hat{\omega}d^2\right]^2\right),\tag{A2}$$

$$F_{\rm d} = 1 - \tanh\left(\left(\frac{c_{\rm dt1}\mu^{\rm t}}{\rho\kappa^2 d^2 \sqrt{2(|S_{ik}|^2 + |W_{ik}|^2)}}\right)^{c_{\rm dt2}}\right),\tag{A3}$$

$$F_{\alpha} = 0.25 - d/\Delta,\tag{A4}$$

$$F_{\rm b} = \min\left[2\exp\left(-9F_{\alpha}^2\right), 1\right],\tag{A5}$$

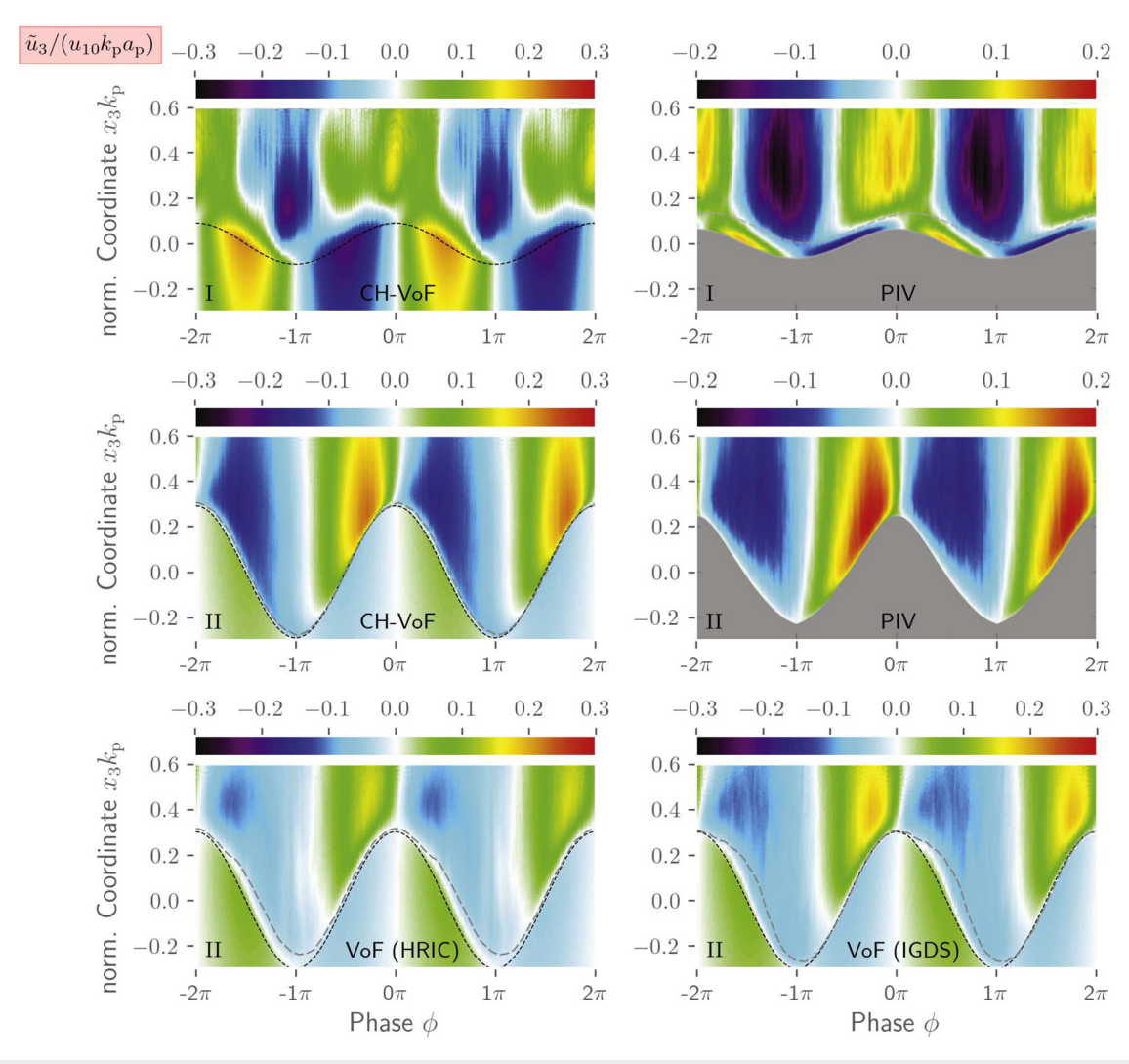


FIG. 17. Similar plots as Fig. 7 with adapted coloring. Reproduced with permission from Buckley and Veron, Eur. J. Mech.-B/Fluids 73, 132–143 (2019). Copyright 2019 Elsevier B.V.

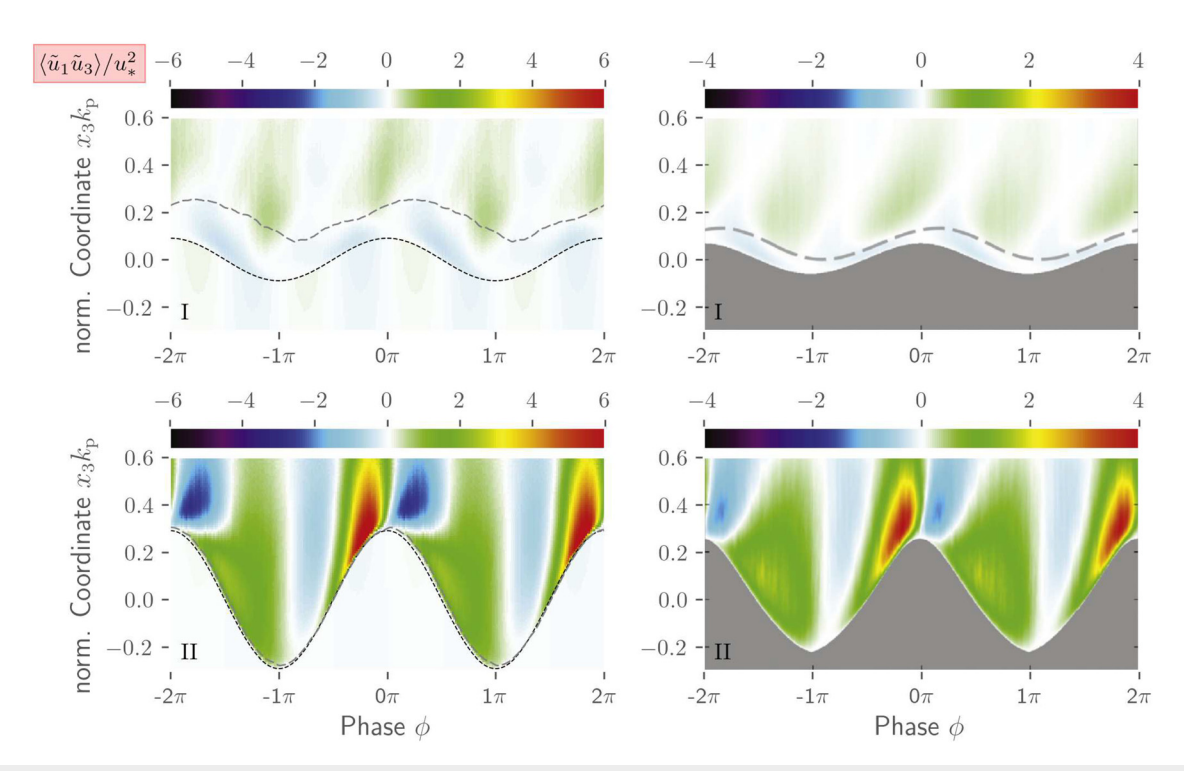


FIG. 18. Similar plots as Fig. 8 with adapted coloring. Reproduced with permission from Buckley and Veron, Eur. J. Mech.-B/Fluids 73, 132–143 (2019). Copyright 2019 Elsevier B.V.

$$\hat{F}_{d} = \max[(1 - F_{d}), F_{b}],$$
 (A6)

$$F_{\rm e} = F_{\rm e2} \max[F_{\rm e1} - 1, 0],$$
 (A7)

$$F_{e1} = \begin{cases} 2e^{(-11.09F_{\alpha}^{2})} & \text{if } F_{\alpha} \ge 0, \\ 2e^{(-9.0F_{\alpha}^{2})} & \text{otherwise,} \end{cases}$$
 (A8)

$$F_{\rm e2} = 1 - \max[F_{\rm t}, F_{\rm l}],$$
 (A9)

$$F_{\rm t} = 1 - \tanh\left(\left(\frac{c_{\rm t}^2 \mu^{\rm t}}{\rho \kappa^2 d^2 \sqrt{2(|S_{ik}|^2 + |W_{ik}|^2)}}\right)^3\right), \tag{A10}$$

$$F_{1} = 1 - \tanh\left(\left(\frac{c_{1}^{2}\mu^{t}}{\rho\kappa^{2}d^{2}\sqrt{2(|S_{ik}|^{2} + |W_{ik}|^{2})}}\right)^{10}\right).$$
(A11)

Table V shows all the parameters used.

APPENDIX B: PLOTS WITH ALTERNATIVE COLORING

For illustration, Figs. 6–8 are recreated with adapted coloring in Figs. 16–18. The reason for the originally chosen representation is due to the measurement data, which is partly only available as images and therefore restricted by the bounds of the colorbar.

REFERENCES

¹C. Wunsch and R. Ferrari, "Vertical mixing, energy, and the general circulation of the oceans," Annu. Rev. Fluid Mech. **36**, 281–314 (2004).

- ²P. P. Sullivan and J. C. McWilliams, "Dynamics of winds and currents coupled to surface waves," Annu. Rev. Fluid Mech. 42, 19–42 (2010).
- ³P. P. Sullivan, M. L. Banner, R. P. Morison, and W. L. Peirson, "Turbulent flow over steep steady and unsteady waves under strong wind forcing," J. Phys. Oceanogr. 48, 3–27 (2018).
- ⁴P. P. Sullivan, J. C. McWilliams, and E. G. Patton, "Large-eddy simulation of marine atmospheric boundary layers above a spectrum of moving waves," J. Atmos. Sci. 71, 4001–4027 (2014).
- ⁵D. Yang and L. Shen, "Direct numerical simulation of scalar transport in turbulent flows over progressive surface waves," J. Fluid Mech. 819, 58–103 (2017).
- ⁶J. B. Edson, V. Jampana, R. A. Weller, S. P. Bigorre, A. J. Plueddemann, C. W. Fairall, S. D. Miller, L. Mahrt, D. Vickers, and H. Hersbach, "On the exchange of momentum over the open ocean," J. Phys. Oceanogr. 43, 1589–1610 (2013).
- ⁷N. Husain, T. Hara, M. Buckley, K. Yousefi, F. Veron, and P. Sullivan, "Boundary layer turbulence over surface waves in a strongly forced condition: LES and observation," J. Phys. Oceanogr. 49, 1997–2015 (2019).
- ⁸C. Hirt and B. Nichols, "Volume of fluid (VoF) method for the dynamics of free boundaries," J. Comput. Phys. **39**, 201–225 (1981).
- ⁹M. Perlin, W. Choi, and Z. Tian, "Breaking waves in deep and intermediate waters," Annu. Rev. Fluid Mech. 45, 115–145 (2013).
- ¹⁰ A. Iafrati, "Numerical study of the effects of the breaking intensity on wave breaking flows," J. Fluid Mech. 622, 371–411 (2009).
- ¹¹A. Iafrati, "Energy dissipation mechanisms in wave breaking processes: Spilling and highly aerated plunging breaking events," J. Geophys. Res.: Oceans 116, C07024, https://doi.org/10.1029/2011JC007038 (2011).
- ¹²P. Lubin and S. Glockner, "Numerical simulations of three-dimensional plunging breaking waves: Generation and evolution of aerated vortex filaments," J. Fluid Mech. 767, 364–393 (2015).
- ¹³Z. Z. Hu, T. Mai, D. Greaves, and A. Raby, "Investigations of offshore breaking wave impacts on a large offshore structure," J. Fluids Struct. 75, 99–116 (2017).
- ¹⁴X. Hao, T. Cao, Z. Yang, T. Li, and L. Shen, "Simulation-based study of wind-wave interaction," Proc. IUTAM 26, 162–173 (2018).

- ¹⁵L. Deike, S. Popinet, and W. Melville, "Capillary effects on wave breaking," J. Fluid Mech. 769, 541–569 (2015).
- 16 J. Wu, S. Popinet, and L. Deike, "Revisiting wind wave growth with fully coupled direct numerical simulations," J. Fluid Mech. 951, A18 (2022).
- ¹⁷J. Cahn and J. Hilliard, "Free energy of a nonuniform system. I. Interfacial free energy," J. Chem. Phys. 28, 258–267 (1958).
- ¹⁸J. Brackbill, D. Kothe, and C. Zemach, "A continuum method for modeling surface tension," J. Comput. Phys. 100, 335–354 (1992).
- ¹⁹P. Hohenberg and B. Halperin, "Theory of dynamic critical phenomena," Rev. Mod. Phys. 49, 435 (1977).
- ²⁰D. Jacqmin, "Calculation of two-phase Navier–Stokes flows using phase-field modeling," J. Comput. Phys. 155, 96–127 (1999).
- ²¹H. Abels, H. Garcke, and G. Grün, "Thermodynamically consistent, frame indifferent diffuse interface models for incompressible two-phase flows with different densities," Math. Models Methods Appl. Sci. 22, 1150013 (2012).
- 22H. Garcke, M. Hinze, and C. Kahle, "Diffuse interface approaches in atmosphere and ocean-modeling and numerical implementation," in *Energy Transfers in Atmosphere and Ocean* (Springer, 2019), pp. 287–307.
- ²³J. Lowengrub and L. Truskinovsky, "Quasi-incompressible Cahn-Hilliard fluids and topological transitions," Proc. R. Soc. London, Ser. A 454, 2617–2654 (1998).
- ²⁴C. Eden and A. Iske, Energy Transfers in Atmosphere and Ocean (Springer, 2019).
- ²⁵N. Kühl, M. Hinze, and T. Rung, "Cahn-Hilliard Navier-Stokes simulations for marine free-surface flows," Exp. Comput. Multiphase Flow 4, 274 (2022).
- ²⁶P. Spalart, S. Deck, M. Shur, K. Squires, M. Strelets, and A. Travin, "A new version of detached-eddy simulation, resistant to ambiguous grid densities," Theor. Comput. Fluid Dyn. 20, 181–195 (2006).
- ²⁷O. Phillips, "On the generation of waves by turbulent wind," J. Fluid Mech. 2, 417–445 (1957).
- ²⁸T. Rung, K. Wöckner, M. Manzke, J. Brunswig, C. Ulrich, and A. Stück, "Challenges and perspectives for maritime CFD applications," Jahrb. Schiffbautechnischen Ges. 103, 127–139 (2009).
- 29S. Yakubov, B. Cankurt, M. Abdel-Maksoud, and T. Rung, "Hybrid MPI/ OpenMP parallelization of an Euler-Lagrange approach to cavitation modelling," Comput. Fluids 80, 365–371 (2013).
- ³⁰N. Kühl, J. Kröger, M. Siebenborn, M. Hinze, and T. Rung, "Adjoint complement to the volume-of-fluid method for immiscible flows," J. Comput. Phys. 440, 110411 (2021).
- ³¹S. Muzaferija and M. Peric, "Computation of free-surface flows using interface tracking and interface-capturing methods," in *Nonlinear Water Wave Interaction* (Wessex Institute of Technology Press, Southampton, 1999), pp. 59–100.
- ³²H. Jasak and H. Weller, "Interface tracking capabilities of the inter-gamma differencing scheme," Technical Report, Department of Mechanical Engineering, Imperial College of Science, Technology and Medicine, University of London (1995).
- 33J. H. Ferziger, M. Peric, and R. L. Street, Computational Methods for Fluid Dynamics (Springer, 2020).

- ³⁴H. Ding, P. D. Spelt, and C. Shu, "Diffuse interface model for incompressible two-phase flows with large density ratios," J. Comput. Phys. 226, 2078–2095 (2007).
- 35O. Ubbink, "Numerical prediction of two fluid systems with sharp interfaces," Ph.D. thesis (Imperial College, 1997).
- 36P. R. Spalart, "Detached-eddy simulation," Annu. Rev. Fluid Mech. 41, 181–202 (2009).
- 37M. Gritskevich, A. Garbaruk, J. Schütze, and F. Menter, "Development of DDES and IDDES formulations for the k-ω shear stress transport model," Flow Turbul, Combust. 88, 431–449 (2012).
- ³⁸F. Menter, M. Kuntz, and R. Langtry, "Ten years of industrial experience with the SST turbulence model," Turbul. Heat Mass Transfer 4, 625–632 (2003).
- ³⁹P. Tucker, "Assessment of geometric multilevel convergence robustness and a wall distance method for flows with multiple internal boundaries," Appl. Math. Modell. 22, 293–311 (1998).
- ⁴⁰A. Belyaev and P. Fayolle, "On variational and PDE-based distance function approximations," in *Computer Graphics Forum* (Wiley Online Library, 2015), Vol. 34, pp. 104–118.
- ⁴¹M. Buckley and F. Veron, "Structure of the airflow above surface waves," J. Phys. Oceanogr. 46, 1377–1397 (2016).
- 42M. Buckley and F. Veron, "Airflow measurements at a wavy air-water interface using PIV and LIF," Exp. Fluids 58, 161 (2017).
- ⁴³M. Buckley and F. Veron, "The turbulent airflow over wind generated surface waves," Eur. J. Mech.-B/Fluids 73, 132–143 (2019).
- ⁴⁴K. Wöckner, W. Drazyk, and T. Rung, "An efficient VoF-based RANS method to capture complex sea states," in *Proceedings of the International Conference* on Offshore Mechanics and Arctic Engineering (ASME, 2010), Vol. 49149, pp. 755–763.
- 45X. Luo-Theilen and T. Rung, "Computation of mechanically coupled bodies in a seaway," Ship Technol. Res. 64, 129–143 (2017).
- ⁴⁶X. Luo-Theilen and T. Rung, "Numerical analysis of the installation procedures of offshore structures," Ocean Eng. 179, 116–127 (2019).
- ⁴⁷T. Hara and P. Sullivan, "Wave boundary layer turbulence over surface waves in a strongly forced condition," J. Phys. Oceanogr. 45, 868–883 (2015).
- ⁴⁸P. P. Sullivan, J. C. McWilliams, and C.-H. Moeng, "Simulation of turbulent flow over idealized water waves," J. Fluid Mech. 404, 47–85 (2000).
- ⁴⁹C. Funke, M. Buckley, L. Schultze, F. Veron, M.-L. E. Timmermans, and J. Carpenter, "Pressure fields in the airflow over wind-generated surface waves," J. Phys. Oceanogr. 51, 3449–3460 (2021).
- 50S. Belcher and J. Hunt, "Turbulent flow over hills and waves," Annu. Rev. Fluid Mech. 30, 507-538 (1998).
- ⁵¹M. Buckley, F. Veron, and K. Yousefi, "Surface viscous stress over wind-driven waves with intermittent airflow separation," J. Fluid Mech. 905, A31 (2020).
- ⁵²J. Carpenter, M. Buckley, and F. Veron, "Evidence of the critical layer mechanism in growing wind waves," J. Fluid Mech. 948, A26 (2022).
- ⁵³A. Ayet and B. Chapron, "The dynamical coupling of wind-waves and atmospheric turbulence: A review of theoretical and phenomenological models," Boundary Layer Meteorol. 183, 1–33 (2022).